7

Synthesis of Nanosized Luminescent Materials and Their Photoluminescence under VUV Excitation

Yuhua Wang, Qizheng Dong, Zhaofeng Wang and Xue Yu
Department of Materials Science, School of Physical Science and Technology, Lanzhou University, Lanzhou, 730000, P. R. China

1. Introduction

Photoluminescence (PL) phosphor can be divided into different types according to the different excitation wavelengths, and they have different applications. The region from 100 to 200 nm is the vacuum ultraviolet (VUV) region and the phosphors excited by VUV light are usually used for plasma display panels (PDPs) and Hg-free lamps.[1] Nowadays, the PDP and liquid-crystal displays (LCDs) are the two most widely used techniques in flat panel display technology. Comparing with LCD, PDP display technique could provide rapider response of pictures, higher contrast and larger viewing angle.[2] Hence, PDP is a promising candidate for the large flat-display industry, especially in 3D displays.

Although PDP are currently available commercially, there are several disadvantages which limited its further application. First of all, PDP has lower luminescent efficiency (Tab. 1). Comparing with several common luminescence techniques, the luminescent efficiency of PDP is lowest.[3]

luminescence techniques	luminescent efficiency (lm/W)
Fluorescent lamp	80 ~ 100
cathode ray tube (CRT)	5 ~ 6
LCD	2 ~ 3.5
PDP	1 ~ 1.5

Table 1. Luminescence efficiency of several luminescence techniques.

VUV commercial phosphor	Applied deficiency	Influences on display
$(Y,Gd)BO_3:Eu^{3+}$	Low color purity (0.641, 0.356)	poor color purity
$BaMgAl10O_{17}:Eu^{2+}$	Low thermal stability (Intensity decrease >15% under 500 °C,10 h)	Shorten useful life
$Zn_2SiO_4:Mn^{2+}$	Long decay time (14.23 ms)	Image delay

Table 2. Main deficiencies of tricolor commercial phosphors for PDP.

Secondly, the representative tricolor commercial phosphors for PDP were (Y, Gd)BO_3: Eu^{3+}, $ZnSiO_4$:Mn^{2+} and $BaMgAl_{10}O_{17}$: Eu^{2+} (BAM). However, there are still some deficiencies in these phosphors: The color purity (Y, Gd)BO_3:Eu^{3+} was poor and the decay time of $ZnSiO_4$:Mn^{2+} was too long for the application, while the instability of BaMgAl10O17:Eu2+ under VUV radiation and thermal treatment was an outstanding problem during panel manufacture (Tab. 2).[4]

What is more, the mechanism of VUV excited luminescence is not clear. The ultraviolet (UV) excited phosphor is usually originated from direct excitation activators. However, the luminescence process under VUV excitation is only considered as the host transfer absorbed excitation energy to activators (Fig. 1).[5] The Specific emission process is not clear. So current research about VUV phosphor focus on these aspects: Improvement on traditional phosphors, development of new phosphors and investigation of luminescence mechanism.

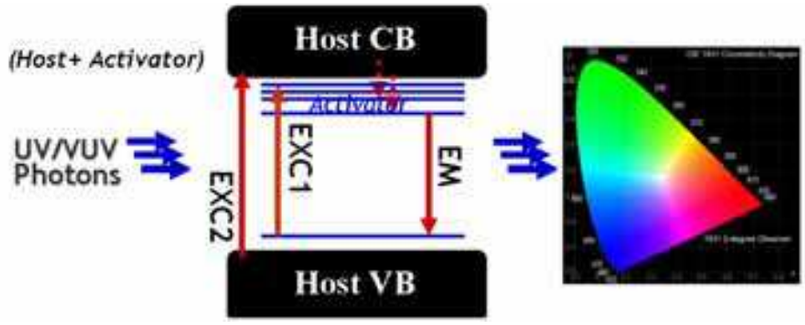

Fig. 1. The luminescence mechanism under UV/VUV excitation.

Recently, many researchers have focused on the preparation and luminescent properties of nano-phosphors because of their different characteristics compared to those of their bulk counterparts. As particles diameter approaches to their Bohr diameter, the optical properties begin to change and quantum confinement effect begins to play a much more important role. It results in great differences in physical and electronic properties between the nanometer-scale particles and bulk materials. Besides, to meet the requirement of the PDP manufacture procedure, nanophosphors were convenient to brush the panel and they could get higher resolution to make the pictures more vivid.[6,7] However, due to restriction on the test equipment, much research about nanophosphors were limited to investigating their optical properties in the UV region. And the optical properties of nanophosphors under VUV excited were scarcely reported. So it is meaningful to investigate the properties of nanophsphors under VUV excitation.

With the expectation of improving the physical, chemical and luminescent properties of ordinary phosphor particles, many soft-chemical techniques have been adopted to synthesize nano-particles on the account of their good mixing of starting materials and relatively low reaction temperature.[8-10] In this work, the nano-scaled tricolor phosphors: YBO_3:Eu^{3+}, $ZnSiO_4$:Mn^{2+} and $BaMgAl_{10}O_{17}$:Eu^{2+}, and other VUV excited phosphors were respectively prepared by different soft-chemical methods, such as solvent-thermal, hydrothermal method and sol-gel process. Our works focus on controlling the size and morphology, improving PL performance and investigating special properties of nanophosphor under VUV excitation. All data in this chapter have been published and all contents are contained in these papers (from ref. 11 to 18).[11-18]

2. Red phosohor of $YBO_3:Eu^{3+}$

$YBO_3:Eu^{3+}$ is a promising red phosphor owing to its high ultraviolet (UV) and VUV transparency, non-linear properties and exceptional optical damage threshold which allows it to withstand the harsh conditions presenting in vacuum discharge lamps or screens.[19] In particular, it exhibits extraordinarily high luminescent efficiency under VUV excitation. However, all of these advantages do not make $YBO_3:Eu^{3+}$ as a desired VUV phosphor because of its poor chromaticity. In the emission spectra of $YBO_3:Eu^{3+}$, the main emission are composed of two transitions: a typical magnetic dipole transition $^5D_0$–$^7F_1$ (orange color), and a typical electric dipole transition $^5D_0$–$^7F_2$ (red color). It is well known that the $^5D_0$–$^7F_2$ transition is hypersensitive to the symmetry of the local crystal fields surrounding the Eu^{3+} ions. When Eu^{3+} ions occupy the inversion sites, according to the selective rule, the magnetic dipole transition is permitted but the electric dipole transition is forbidden, and then causes a poor chromaticity, which is to say that the color purity of the $YBO_3:Eu^{3+}$ would improve by decreasing the particle size of the $YBO_3:Eu^{3+}$ phosphor.[20,21]

2.1 Controllable morphology of $YBO_3:Eu^{3+}$ nanophosphors

Reports about preparing various morphologies and sizes of $YBO_3:Eu^{3+}$ are scarce. Because the natural growing habit of YBO_3 is sheet-like,[22-24] which always plays an important role in determining the final morphology of $YBO_3:Eu^{3+}$. In addition, $YBO_3:Eu^{3+}$ are apt to form highly agglomerated particles[25] and it is the ''thermodynamic-stable species'' that could only be obtained under harsh conditions, so no efficient control over their size and morphology has been achieved yet.[24] Many works have been reported for preparing the different morphology and size of $YBO_3:Eu^{3+}$ nanophosphor.[20,24,26-28] However, there is no report about preparing various morphologies and sizes of $YBO_3:Eu^{3+}$ only by adjusting one reaction condition in one simple method. In this paper, we first prepared multifarious morphologies and sizes of $YBO_3:Eu^{3+}$ by adjusting the pH value of precursors in hydrothermal reaction (HR) method at a low temperature of 260 1C for 3 h, in the absence of any surfactant and template, without milling and post calcination. The relationships between pH value of precursors and samples' morphologies, sizes, were discussed.

Samples pH	Mean grain size (nm)
6	25.1
7	19.1
8	17.7
9	23.5
9.5	68.2
10	238.2
11.28	475.0

Table 3. Mean grain sizes of samples.

As shown in Fig. 2, most diffraction peaks of HR samples display a broadening behavior and quite different intensities compared with those of Solid state Reaction (SR) sample. It indicates that the morphologies and sizes of HR samples have great changes. The particle

size can be estimated from the Sherrer equation. The calculated mean grain sizes are listed in Tab. 3. It should be stated that the Sherrer equation is tenable when the grain size is less than 100 nm. Hence, the calculated values which are more than 100nm can only be employed to do qualitative analysis. With the pH values of precursors going on increasing, the mean grain sizes increase dramatically. For sample 9.5, the size increases to 68.2 nm. Samples 10 and 11.28 are no longer in nanoscales.

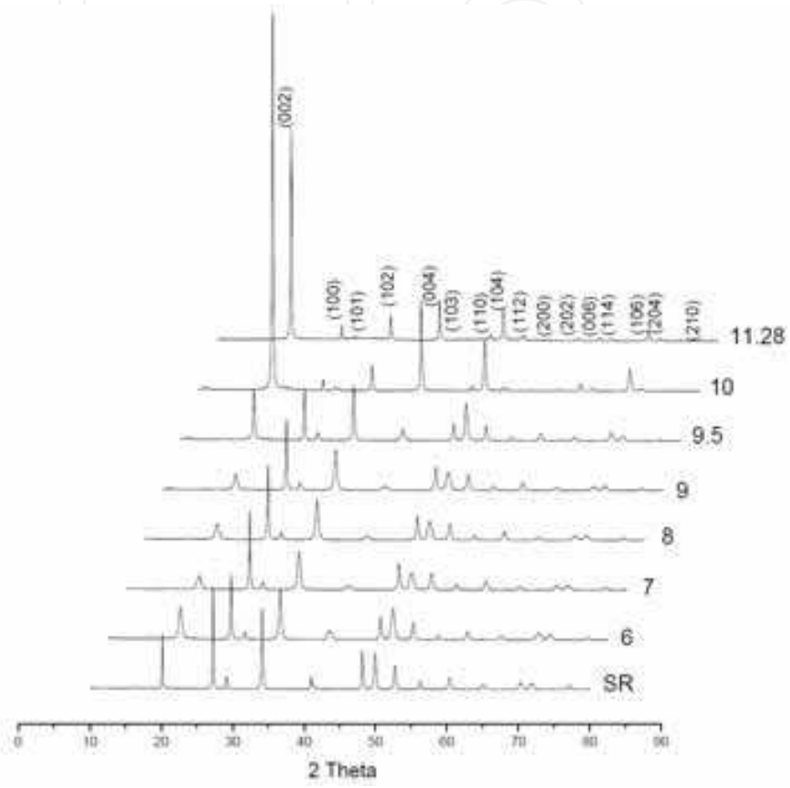

Fig. 2. XRD patterns of all $YBO_3:Eu_{0.05}$ samples

Fig. 3a shows the typical TEM image. The particles are irregular sheet-like and decrease to nano-sized. Their thicknesses are estimated to 20–40nm and the planar sizes are distributed in the range 40–120 nm. The typical FE-SEM images of sample 6 are exhibited in Fig. 3b and c. The sheet-like nano-particles are clearly observed. Fig. 4a exhibits the typical TEM image of sample 7. These particles are similar to those of sample 6. However, the typical FE-SEM images (Fig. 4b and c) clearly show that these small nano-sheets are apt to connect each other in one layer to form some bigger nano-sheets, whose thickness are still nano-size but planar sizes can reach to microsize.

Fig. 5 displays the typical TEM image and FE-SEM images of sample 8. In this sample, the aforementioned bigger nano-sheets assemble more tightly that make clusters like blooming flowers and downy balls. Most clusters are about 6–8 mm. Fig. 6a exhibits the typical TEM image of sample 9. The nano-sheets show stronger tendency to agglomerate with each other. Correspondingly, it can be clearly observed in the FE-SEM image (Fig. 6b) that all the nano-sheets assemble to form blooming flower-like clusters with sizes about 4–5 mm, which are somewhat smaller than those of sample 8.

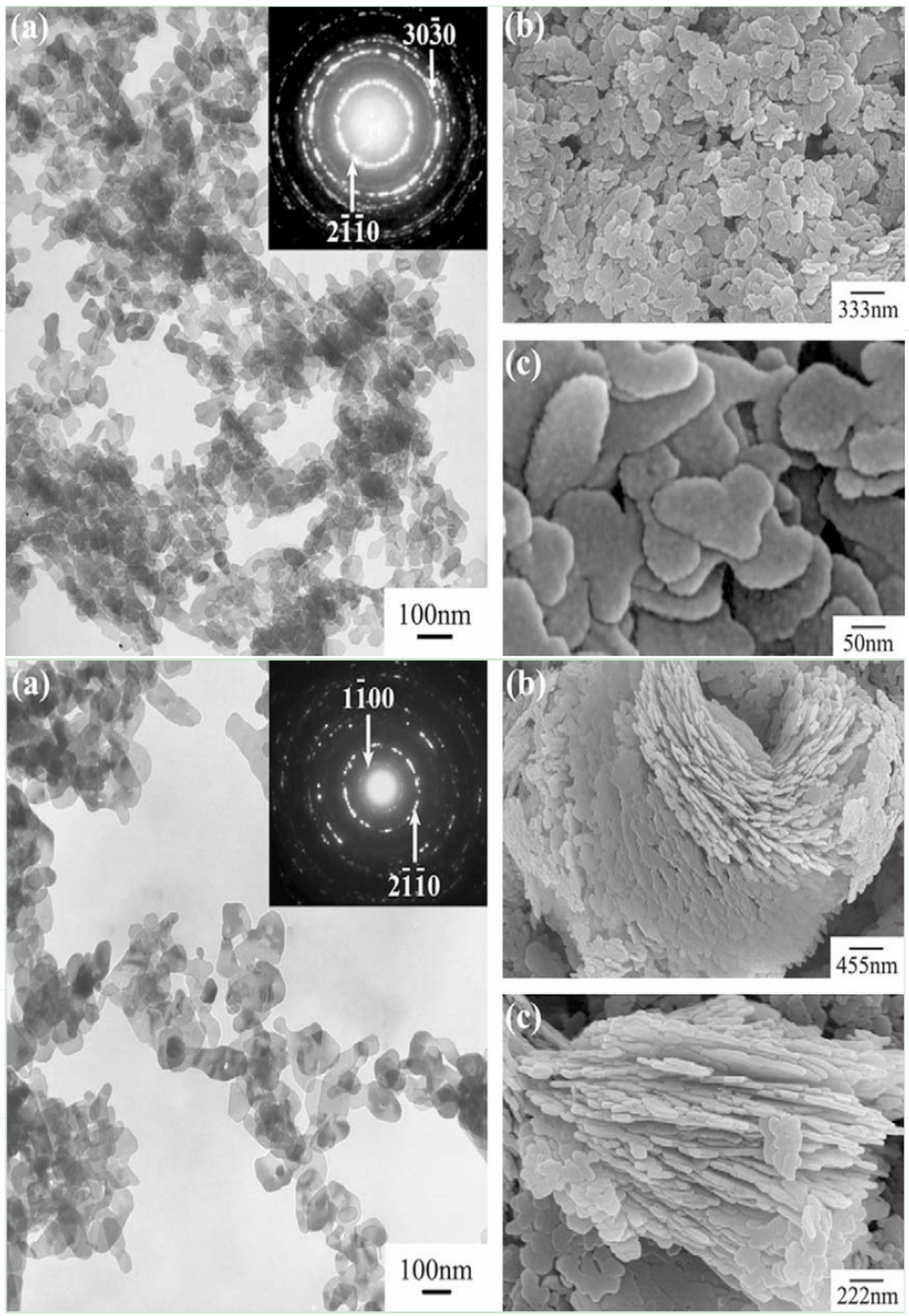

Fig. 3 (above). and 4 (botom). Electron microscopy images of $YBO_3:Eu_{0.05}$ sample prepared by HR method with precursor pH=6 (sample 6, Fig. 3) and 7(sample 7, Fig. 4). (a) TEM and SAED images. (b,c) FE-SEM images.

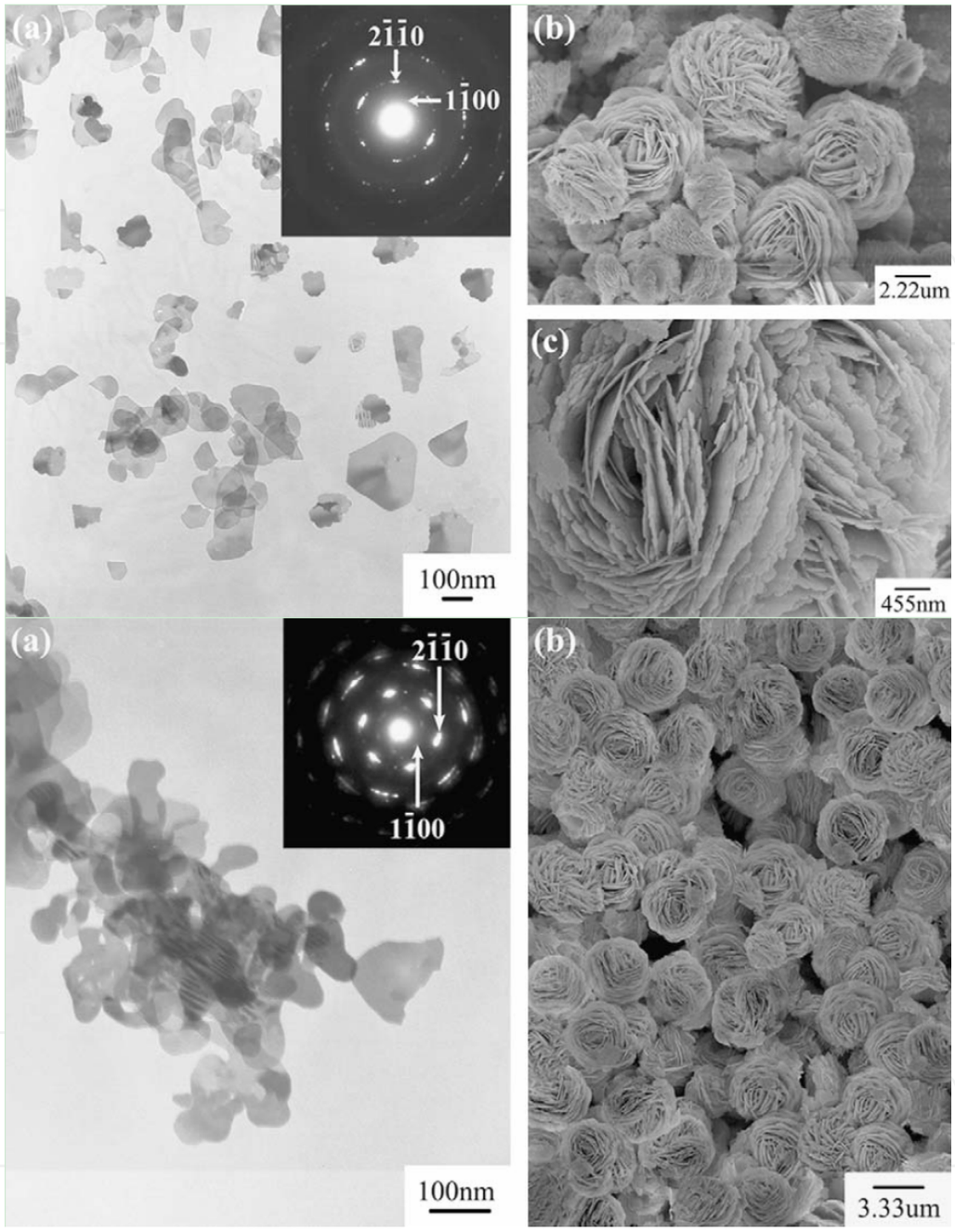

Fig. 5 (above). and 6 (botom). Electron microscopy images of $YBO_3:Eu_{0.05}$ sample prepared by HR method with precursor pH=8 (sample 8, Fig. 5) and pH=9 (sample 9, Fig. 6). (a) TEM and SAED images. (b,c) FE-SEM images.

As shown in Fig. 7, particles' morphology and size change dramatically for sample 9.5. Some particles change to rod-like whose diameters are distributed in the range 200–1500nm and the lengths are about 5–20 mm, others grow into bigger sheets with planar sizes about 3–20 mm. With precursor pH value increasing to 10, more rod-like particles form (Fig. 8). At the same time, the sheets still exist in the products, and their planar sizes increase to 5–30

mm. The aspect ratios of most rods are higher than those of sample 9.5, for their lengths increase to 10–50 mm range but diameters change little.

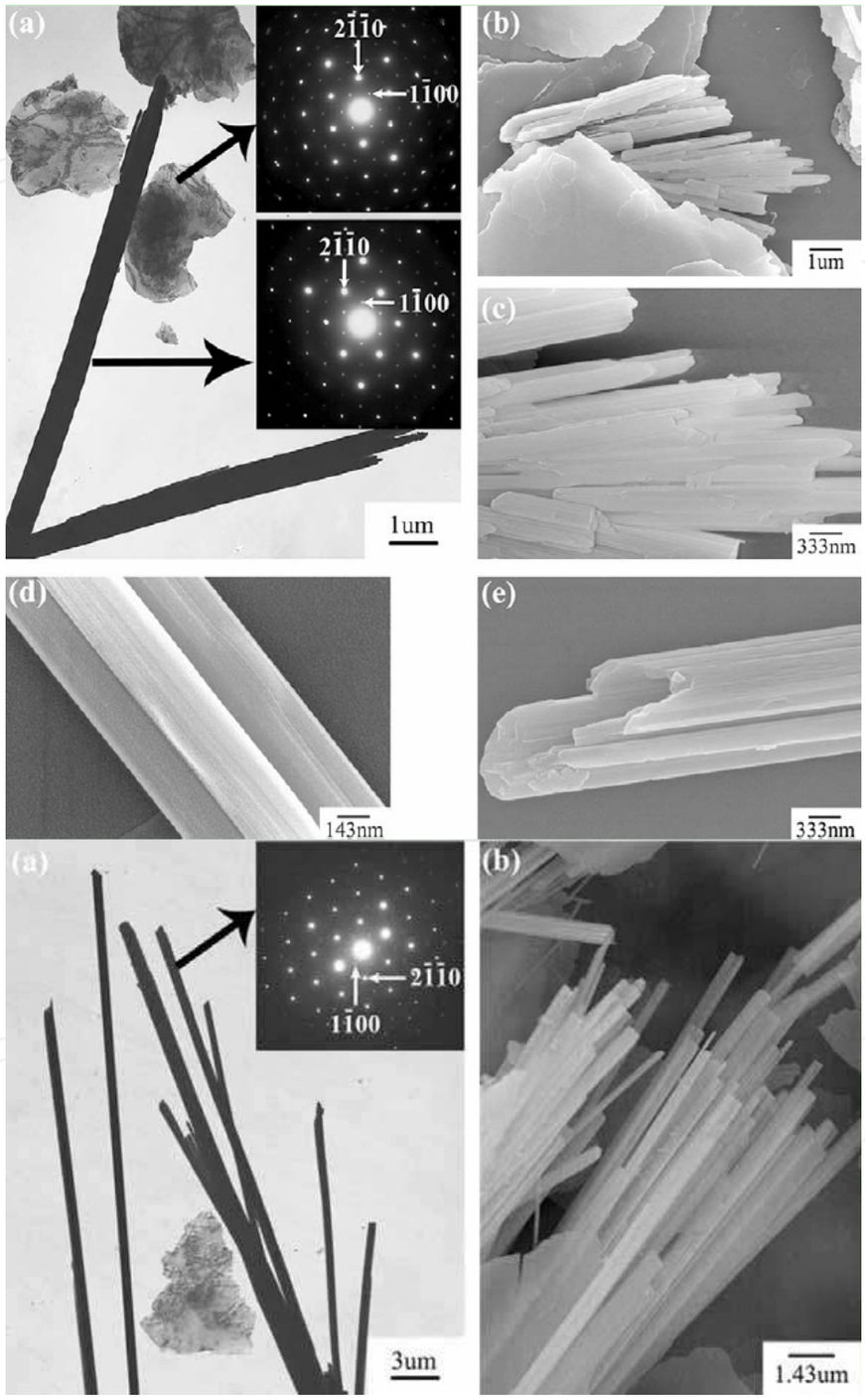

Fig. 7 (above). and 8 (botom). Electron microscopy images of $YBO_3:Eu_{0.05}$ sample prepared by HR method with precursor pH=9.5 (sample 9.5, Fig. 7) and pH=10 (sample 10, Fig. 8). (a) TEM and SAED images. (b–e) FE-SEM images.

When the pH value of precursor increases to 11.28, which is the highest value that can be adjusted in our experiment, the morphologies and sizes of the particles change dramatically once more as Fig. 9 shown. The rod-like particles are replaced by lots of uniform, non-aggregated, quasi-spherical, nano-sized particles with the diameters about 20–30 nm. Some nano-sheets still exist in this sample. Both sheet-like and quasi-spherical particles are monocrystallines.

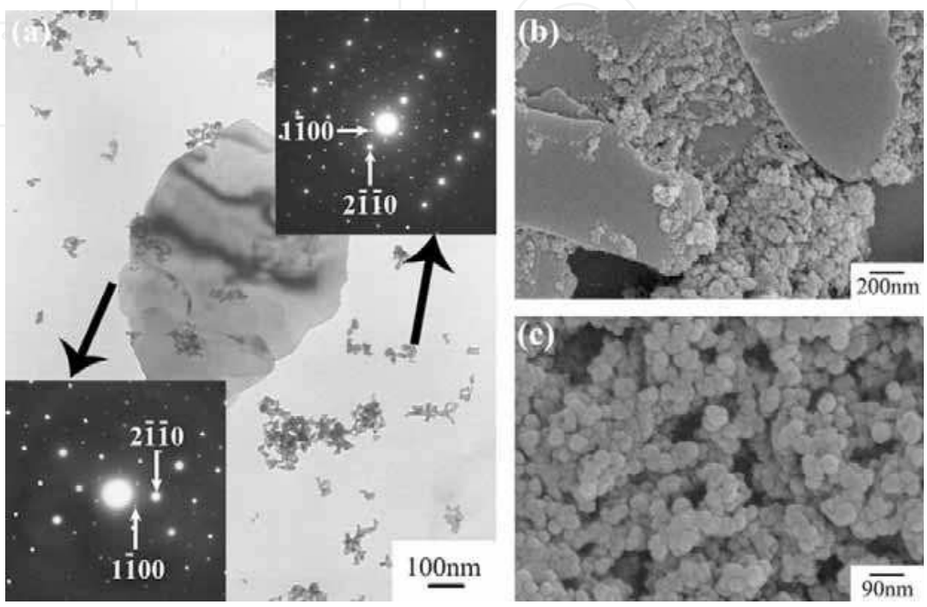

Fig. 9. Electron microscopy images of YBO_3:$Eu_{0.05}$ sample prepared with precursor pH=11.28 (sample 11.28). (a) TEM and SAED images. (b,c) FE-SEM images.

In conclusion, the XRD, TEM and SEM give the accordant result about the morphologies and sizes of all samples. For HR samples, the particles' morphologies and sizes intensively depend on the pH value of the precursors, and particles have a tendency to form monocrystallines with increasing the pH.

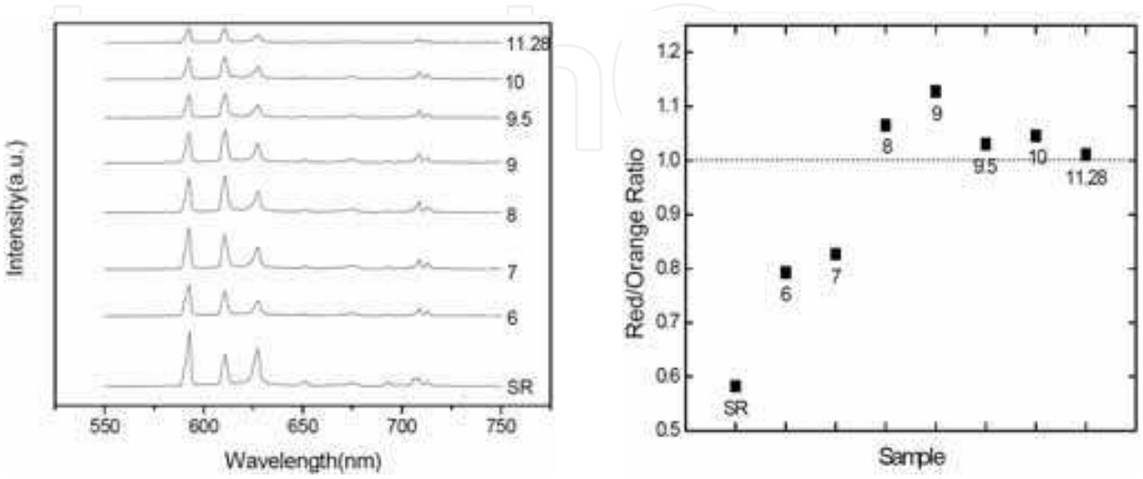

Fig. 10. (a) Emission spectra of all YBO_3: $Eu_{0.05}$ samples; (b) R/O of all YBO_3: $Eu_{0.05}$ samples

All samples were investigated their PL properties under 147nm excitation and the emission spectra was showed in Fig. 10. All spectra in Fig. 10 consists of sharp lines ranging from 580 to 700 nm, which are associated with the transitions from the excited $^5D_0$ level to ^7F_J (J=1, 2, 3, 4) levels of Eu^{3+} activators.[29,30] The major emissions of $YBO_3:Eu^{3+}$ is at 592 nm ($^5D_0 \rightarrow {}^7F_1$) and 611 and 627 nm ($^5D_0 \rightarrow {}^7F_2$), which correspond to orange and red color, respectively. It is well known that the relative intensity of $^5D_0 \rightarrow {}^7F_1$ transition (orange light) or $^5D_0 \rightarrow {}^7F_2$ transition (red light) depends strongly on the local symmetry of Eu^{3+} ions. When Eu^{3+} ions occupy the inversion center sites, the $^5D_0 \rightarrow {}^7F_1$ transition should be relatively strong and when Eu^{3+} ions occupy the lower symmetry site, the $^5D_0 \rightarrow {}^7F_2$ should be relatively strong.[20] As seen in the emission spectrum of SR samples, the peak at 592 nm is dominant. Whereas in our hydrothermal samples, the $^5D_0 \rightarrow {}^7F_2$ transition located at 611 nm is strongest. The emission intensity at 611 nm increase as pH value, and reach to the strongest when pH=9. It indicates better color purity. The color purity of Eu^{3+} doping phosphors can be characterized as the intensity ratio between the red emission ($^5D_0 \rightarrow {}^7F_2$) and the orange emission ($^5D_0 \rightarrow {}^7F_1$) (R/O ratio). The R/O ratios of these samples are shown in Fig. 10b. It can be seen the nanosized $YBO_3:Eu^{3+}$ have higher R/O ration than bulk samples (SR). When PH=9, the emission intensity and (R/O) ratio reach to the highest.

2.2 Improvement PL performance of $YBO_3:Eu^{3+}$ nanophosphors

From above section, we got the different size and morphology of nanosized $YBO_3:Eu^{3+}$ by adjusting the PH value. What is more, the PL properties could also be adjusted. However, the nanophosphor has relatively lower luminescence intensity comparing with their bulk counterparts, which is due to milder synthesis condition leading to the nanopaticles with lower crystallinity and high surface defects density. So the further thermal treatment is needed to increase the PL intensity. However, nanophosphors usually would agglomerate after thermal treatment, which means that the morphology was broken and the particle size growth up. For $YBO_3:Eu^{3+}$, the color purity would decrease as particle size growth up.

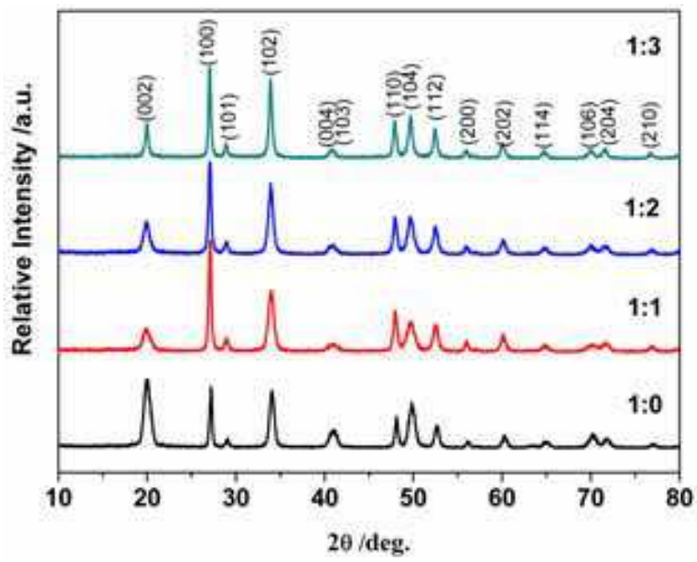

Fig. 11. XRD patterns of the $YBO_3:Eu^{3+}$samples prepared with different ratios of water to solvent

On the other hand, the ideal phosphor would have the smaller size, high luminescence intensity, good color purity and well dispersion. In order to reach these purposes, some solvent was added during the reaction process. It used to control the particle size during the reaction process and keep the morphology during the heat treatment.

Fig. 11 shows XRD patterns of the samples synthesized with different ratios of water to solvent. All the diffraction peaks could be indexed to the JCPDF card (No. 83-1205), and there is no second phase observed. As shown in the Fig.11, the relative intensity of the diffraction peaks for the solvent-thermal (SO) samples are different from the sample prepared by hydrothermal reaction (HR, the 1:0 samples). The (002) peak is the strongest for the HR samples but the (100) peak becomes strongest when the solvent was introduced in the reaction systems, indicating the appearance of a preferred orientation.

The TEM photographs of the SO and HR samples are shown in Fig. 12. In Fig. 12a, we could find that the HR particles are rod-like with size of 150nm in diameter and 300nm in length. By the addition of solvent, the morphology changes into nano-sheets and the size is less than 50 nm. The particles in SO sample also represents better dispersion than that of HR samples. The morphology change here is consistent with the change of preferred orientation in XRD patterns. This result indicates that adding solvent will be conducive to decrease grain size and improve dispersion of the sample particle. It is accepted that nanoparticles crystallized by the dissolution–reprecipitation mechanism during the hydrothermal reaction,[31] and this mechanism is also suitable for our system. Solvent and water present different physical properties. With the addition of solvent to the aqueous solution, the dielectric constant of the mixed solvent decreased, and led to the decrease in solubility of the reaction materials during the crystallization process. As a result, this led to the formation of smaller particles.[32]

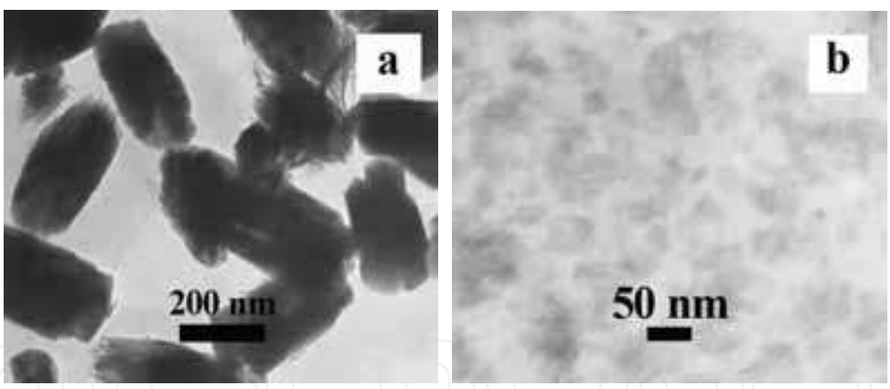

Fig. 12. The TEM images of YBO3: Eu3+ phosphors prepared by different reation. (a) HR Samples; (b) SO samples

Under 147nm excitation, the emission spectra of the SO samples with different ratios of water to solvent are shown in Fig. 13. It is observed that the strongest red emission is at the water to solvent ratio of 1:2, and the PL intensity of 1:3 samples is lower obviously than the others. It can be due to the existence of a small amount of OH^- coordinated to lanthanide ions at the surface of phosphors prepared by the wet chemical method. Adding excessive amount organic solvent (over 1:3) lead to large number of OH^- adhering on the surface of phosphor, which result in the poor PL intensity.[33] As can be seen in the figure, the $^5D_0 \rightarrow {}^7F_2$ emission increased and $^5D_0 \rightarrow {}^7F_1$ emission decreased with solvent added. This must be associated with particle size of samples (observed before). It is well known that the relative intensity of $^5D_0 \rightarrow {}^7F_1$ transitionor $^5D_0 \rightarrow {}^7F_2$ transition depends strongly on the local symmetry

of Eu^{3+}. When the particle size decreases, smaller particles have more effective surface area and more lattice distortion, leading to many Eu^{3+} ions occupying lower symmetry sites. This will increase the transition probability of $^5D_0 \rightarrow {}^7F_2$ and thus improve color purity.[20] It was found that the ratio of red emission (611nm) intensity to orange emission (592nm) intensity (R/O) is 1.11 for the 1:2 sample, which is the highest value among above samples. It predicts that the SO sample (solvent at 1:2) has the best color purity. The R/O ratios, chromaticity coordinates and relative luminescence intensity under VUV excited of the optimum samples were listed in Tab.4. As seen, the optimum nanophosphor sample has a better R/O ration and chromaticity coordinates is better than bulk and commercial red phosphor KX-504A. Meanwhile, the relative intensity was close to the bulk phosphor.

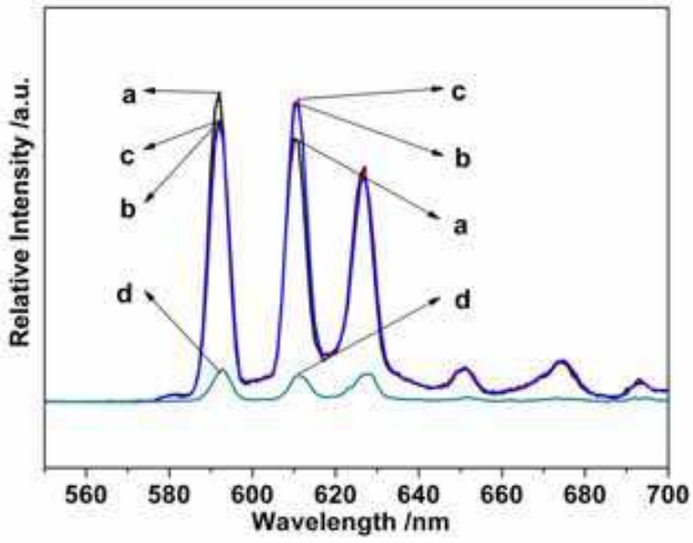

Fig. 13. Emission spectra of $YBO_3:Eu^{3+}$ nano-phosphors prepared at different ratios of water to solvent. (a) 1:0; (b) 1:1; (c) 1:2; (d) 1:3 (λ_{ex}=147nm)

	R/O	X	Y	I%
		(λ_{ex}=147nm)		
NTSC		0.67	033	
KX504	0.69	0.644	0.355	100%
bulk	0.66	0.641	0.358	81.15%
Optimum sample	1.10	0.645	0.354	78.83%

Table 4. The R/O ratios and Chromaticity coordinates of the nano sample and bulk sample

2.3 Unique PL properties of $YBO_3:Eu^{3+}$ nanophosphors under VUV excitation

In the above section, we got the $YBO_3:Eu^{3+}$ nanophosphor with controllable morphology and size, and its PL performance was also improved. Meanwhile, as the nanophosphor, it should have many unique PL properties under VUV excitation comparing with bulk phosphor. A phosphor under VUV excitation has different PL mechanism comparing with that under UV excitation. This will be possible to generate some novel phenomena in nanophosphors. Here, we adopt a low temperature hydrothermal method without further treatment process to obtain $YBO_3:Eu^{3+}$ nanophosphors. With controlling the reaction times,

we got the $YBO_3:Eu^{3+}$ nanophosphors with different grain size. Through compare the different between UV and VUV spectra, we initially obtain the unique PL phenomenon under VUV excitation.

Fig. 14 shows XRD patterns of $YBO_3:Eu^{3+}$ samples synthesized with hydrothermal reaction (HR) for different times. All samples were well-crystallized, and they could all be recognized as single phase in terms with JCPDF (83-1205). No second phase was observed. The relative intensities of different peaks changed with holding times. The intensity ratio of (100) to (102) increased as time increased from 3 to 9 h. The (100) peak, usually the strongest in these samples, became the third strongest in the 9 h samples. When the holding time was extended from 9 to 15 h, the (100) peak became the strongest again. The intensity ratio between other peaks, such as (002) to (100) and (110) to (104), also changed with extended time. This shows that the preferred orientation has been changed. By using the Scherrer formula to calculate grain size from each diffraction peak of the samples and average the results was showed in Tab. 5., it can be found that all of these samples reached nanoscale, and the grain sizes did not change significantly with increased holding time (24.99–26.59 nm). This suggests that we could get nanosized $YBO_3:Eu^{3+}$ phosphor lasting only 3 h. With increasing holding time, the crystallinity and grain size do not transform obviously, but the preferred orientations change.

Samples	average grain size (nm)
3h	26.03
6h	26.06
9h	25.76
12h	26.59
15h	24.99
SR	>100

Table 5. Average grain size of HR samples

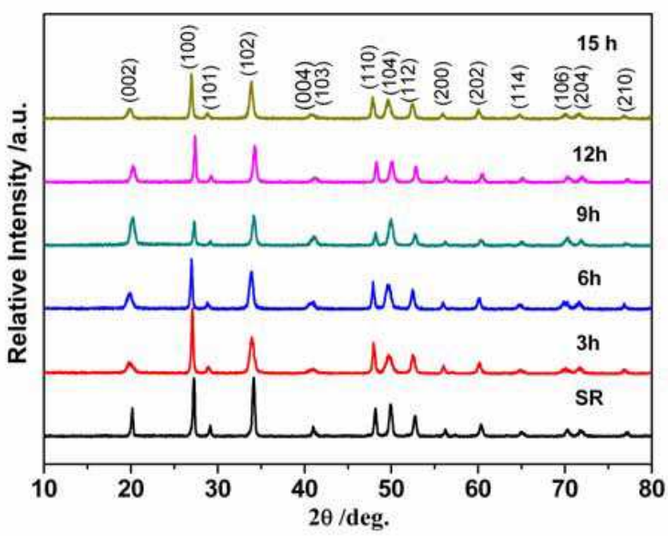

Fig. 14. XRD patterns of $YBO_3:Eu^{3+}$ samples synthesized by different times.

The SEM photographs of the 3 and 9 h samples are shown in Fig. 15, and the TEM photographs are shown in Fig. 16. As can be seen in Fig. 15, the two samples consist of nanosheets, but the morphology and aggregation states are different. The nanosheets in the 3 h sample regularly aggregate into rose-like spherules, and the diameter of each spherule is about 2–3 μm (Fig. 15a and c). In the 9 h samples, they loosely aggregate together without order (Fig. 15b and d). In the TEM photographs (Fig. 16), the size of particles in the 3 h sample is about 300 × 150 nm (Fig. 16a). This differs from calculated results from XRD, indicating that a particle in this sample is polycrystalline and consists of several monocrystalline particles (Fig. 16a). In the 9 h sample (Fig 16b), many particles are nanosheets approximately 50–100 nm long and much thinner. Linking with the SEM, we can find orderly morphology is formed in a shorter time (3 h), but this morphology is broken and the aggregation state is dispersed when the time is extended to 9 h. This indicates that a recrystallization process is likely to exist with holding time change, and it could explain the relative intensities of diffraction peaks changed in XRD section. From above results, we can consider the particle size gradually decreases in this period of time (3–9 h).

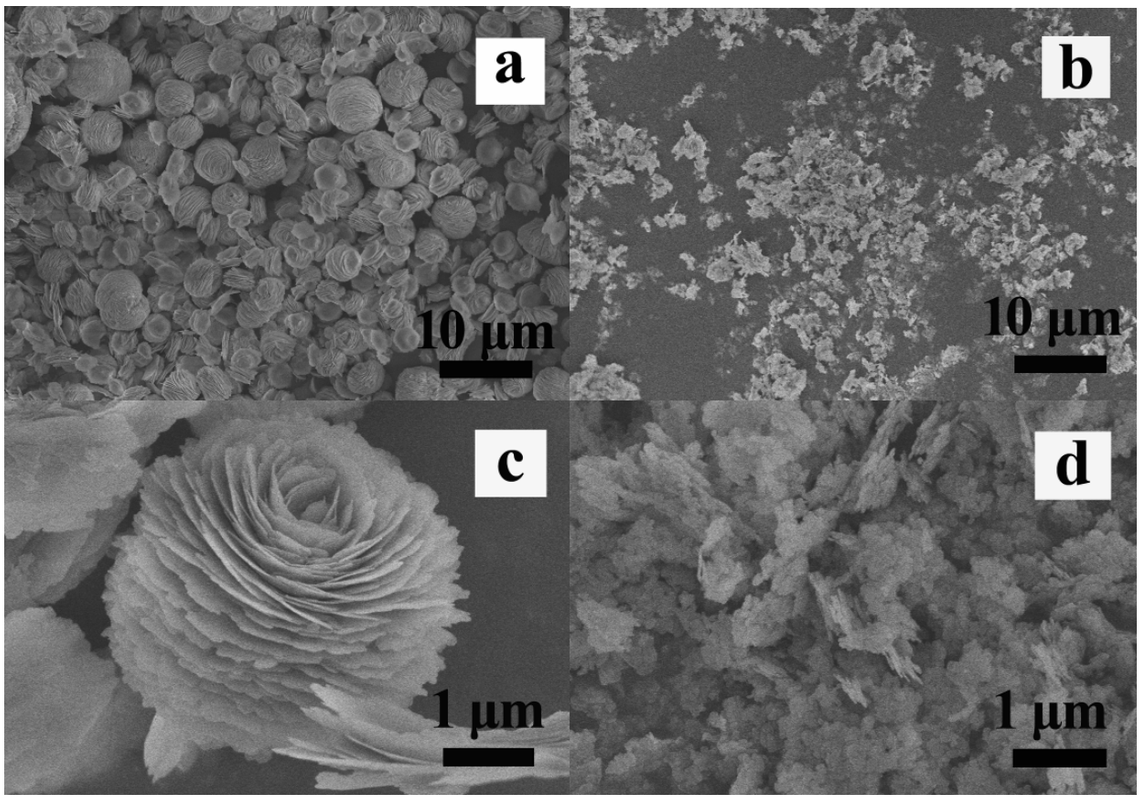

Fig. 15. SEM photographs of $YBO_3:Eu^{3+}$; (a) and (c), 3h sample; (b) and (d) 9h sample.

The VUV excitation spectra of 3, 6, and 9 h samples are presented in Fig. 17. The excitation spectra consisted of several bands in the range of 120–260 nm. The bands in the region from 190 to 260 nm could be result from the overlapping of two bands. One is located at 222 nm and probably is related to an excitonic transition (ET) from the O2*p* state to the Y (4*d* + 5*s*) state.[34,35] The second band occurring around 237nm is known to be a charge-transfer (CT) process, which is related to an electron from the O 2*p* state to Eu^{3+} 4*f* state.[36] In the region from 120 to

190 nm, two bands are overlapped. One is the BO_3 group absorption (BA) band (peak at about 145 nm) and the other is the Eu^{3+} 4*f*-5*d* transition band (peak at about 154 nm).[5]

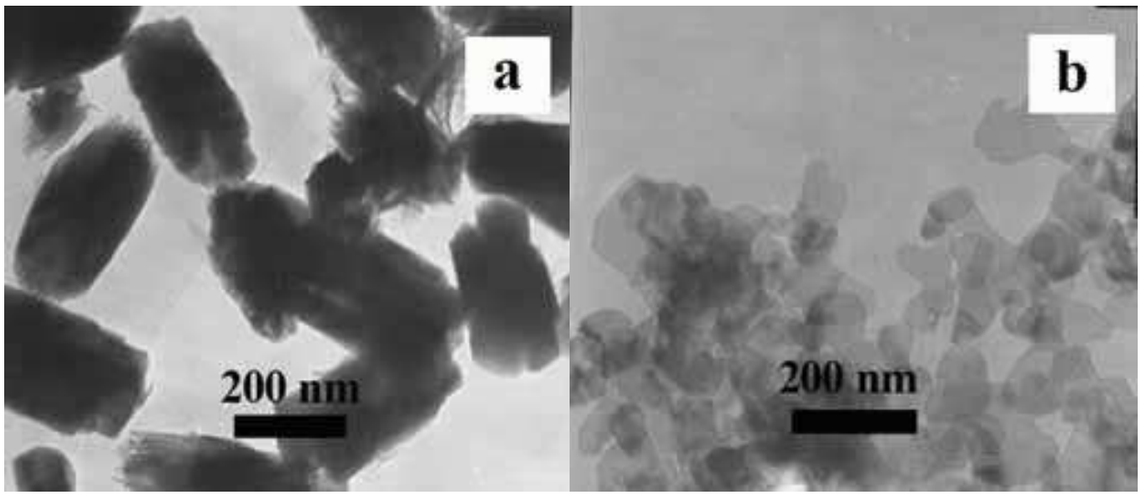

Fig. 16. TEM photographs of $YBO_3:Eu^{3+}$; (a) 3h sample; (b) 9h sample.

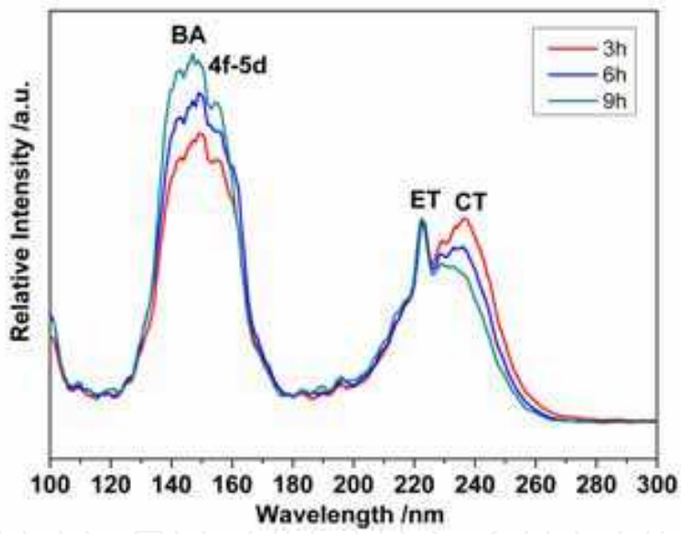

Fig. 17. VUV excitation spectra of $YBO_3:Eu^{3+}$ from 3h to 9h.

As for the bulk and submicrosized $YBO_3:Eu^{3+}$ samples, only one band could be observed in the region from 190 to 260 nm because the two bands are overlapped. However, in the nanosized $YBO_3:Eu^{3+}$ sample, as can be seen in Fig. 17, a blueshift of the ET band and a redshift of the CT band could be observed, and as a result, these two bands separated and could be distinguished. The phenomena could be explained by quantum size effects.[21] With increased holding time, the position of the ET band did not change, but the blueshift of CT band was observed. The phenomena could be explained by quantum size effects.[37] Furthermore, with the particle size decreased (from 3 h to 9 h), the intensity of the CT band became weaker, but the ET band did not change evidently. The same phenomenon was observed in $Y_2O_3:Eu^{3+}$ sample,[38] due to surface effects in the nanophosphor and the

absorption properties of CT and ET bands. At the same time, the intensity of the BA band became stronger. This can be considered to be caused by particle decrease. As is universally known, UV light has a large penetration depth for phosphors (several microns) but VUV light has a small penetration depth (<100 nm).[39] Therefore, the BA process could only occur close to the surface of the phosphor. With the size decrease, more areas could be irradiated, and VUV transparency increased, leading to the increased BA process. For nanophosphor, the small penetration depth of VUV light is an important factor to affect the PL properties, which usually lead totally different PL performance between UV excitation and VUV excitation. We have discovered a unique phenomenon about nanophosphor, which could be explained by the "self-purification" effect in nanosystems. And we made further discuss about the relationship between penetration depth of VUV light and VUV PL performance of nanophosphors.[40]

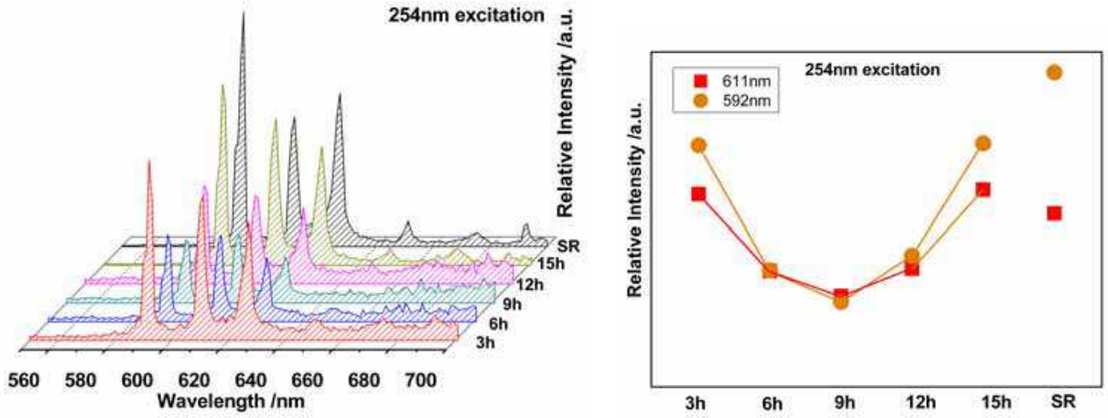

Fig. 18. Emission spectra of $YBO_3:Eu^{3+}$ (λ_{ex}= 254 nm) (a) different time HR samples and SR sample, (b) schematic diagram of intensity change.

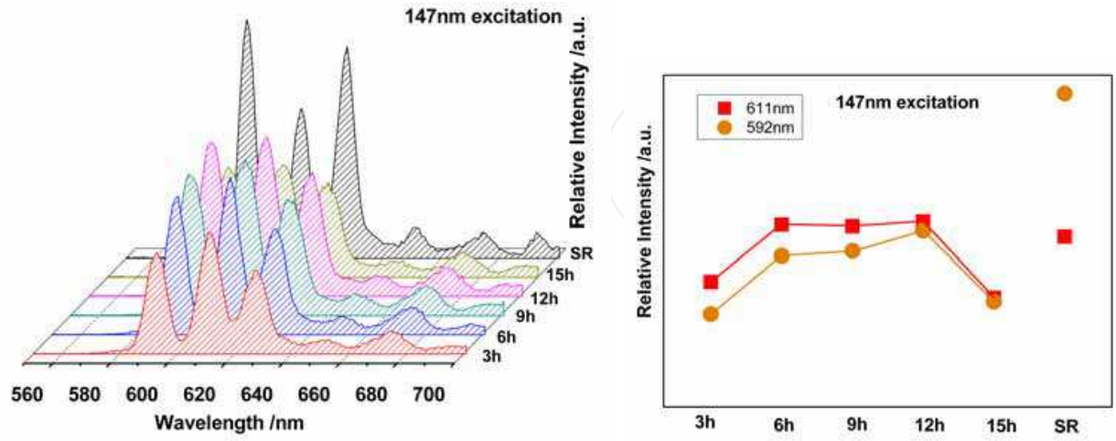

Fig. 19. Emission spectra of $YBO_3:Eu^{3+}$ (λ_{ex}= 147 nm) (a) different time HR samples and SR sample, (b) schematic diagram of intensity change.

Figs. 18 and 19 show the emission spectra under 254 and 147 nm excitation. For nanoscale $YBO_3:Eu^{3+}$ phosphors compared to bulk $YBO_3:Eu^{3+}$, the $^5D_0 \rightarrow {}^7F_2$ transition is usually

relatively stronger because smaller particles have more effective surface area and more lattice distortion, leading to many Eu^{3+} ions occupying lower symmetry sites.[3, 4] Figs. 18b and. 19b show the change trend of relative emission intensity at 592 and 611 nm under UV and VUV excitation. Several interesting phenomenon should be noted. Under 254 nm excitation, the luminescence intensity of HR samples decreased first and increased later (Fig. 18a and b). However, the emission under VUV excitation increased first and decreased later (Fig. 19a and b). For instance, the 3 h sample and 15 h sample have the strongest intensity in the series samples under UV excitation, but under VUV excitation, they are almost the lowest. From XRD and electron microscopy results, we could consider that the particle sizes of the YBO_3:Eu^{3+} phosphor decrease and then increase from 3 to 15 h, owing to a recrystallization process. These results show that in a certain nanoscale, the luminescent intensity under VUV excitation would increase but under UV excitation would decrease as the size decreased.

3. Green phosphor of Zn_2SiO_4: Mn^{2+}

Zn_2SiO_4: Mn^{2+} has been widely used as an efficient green phosphor in plasma display PDPs, CRT, field emission displays (FED), backlight of LCD and electroluminescence (EL) devices due to high luminescent efficiency and chemical stability.[41-44] As far as the synthesis processes concerned, this phosphor was usually prepared by the solid-state reaction method, which involves a pulverizing process and subsequent high-temperature firing, and the resulting Zn_2SiO_4: Mn^{2+} powder possess diameters of about 2 and 20 μm with irregular shape.[45,46] Recently, for advancing display device technology, fine particle phosphors with smaller size and more uniform shape than those commercially available phosphors are in urgent need.[47-50] It is of interest to prepare nanoscaled phosphor to improve the dispersion and luminescence properties.[51] Additionally, nanoscaled phosphor materials offer the potential for preparing smoother films with higher packing densities than conventional micron-sized phosphors.[1,45] Many new methods for the preparation of Zn_2SiO_4: Mn^{2+} has been proposed, including sol–gel,[52] spray pyrolysis[53] and hydrothermal method.[54] Among these synthesis methods, hydrothermal processing has great advantages, such as low processing temperature at high pressure, better metal ions distribution and lower cost.[55] Therefore, we synthesized Zn_2SiO_4: Mn^{2+} nanoscaled phosphor at a low temperature via hydrothermal route, and their PL properties under VUV excitation were evaluated.

3.1 Controllable morphology of Zn_2SiO_4: Mn^{2+} nanophosphors

Fig. 20 shows the XRD patterns of Zn_2SiO_4:Mn^{2+} phosphors prepared at different temperatures for 4 hours. All the diffraction peaks can be indexed to pure hexagonal-structured Zn_2SiO_4 (JCPDS card No.37-1485). No obvious impurity phase was detected. The XRD result shows that pure hexagonal-structured Zn_2SiO_4 can be obtained at a low temperature of 140°C, which is lower than that of 220°C reported by Wan et al.[55] and much lower than using the conventional solid-state reaction method. The XRD pattern in Fig. 21 exhibits that samples heated for different time are almost pure phase of Zn_2SiO_4. The crystal structure had no obvious change as the sample was heated from 1 to 8 hours at 220°C. The $Zn_4Si_2O_7(OH)_2H_2O$ is not detected as reported by the Ref.,[56] which means that there is no intermediate phase in our hydrothermal procedure. The average crystallite sizes estimated from the Scherrer equation indicated all the samples were in nanoscaled.

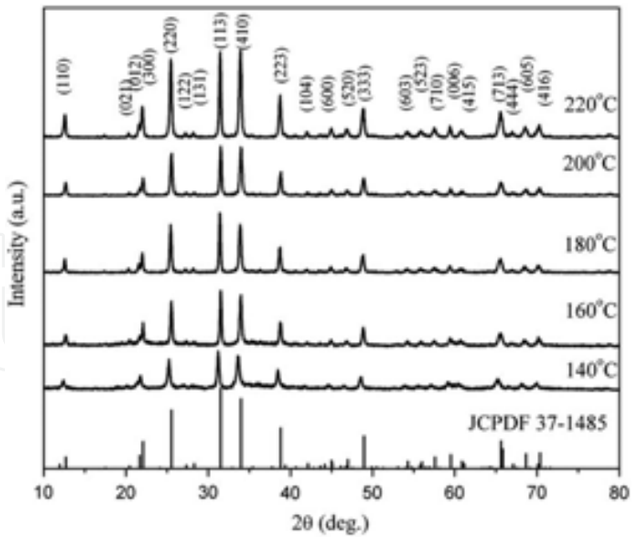

Fig. 20. XRD patterns of the Zn_2SiO_4: Mn^{2+} samples prepared at different temperatures.

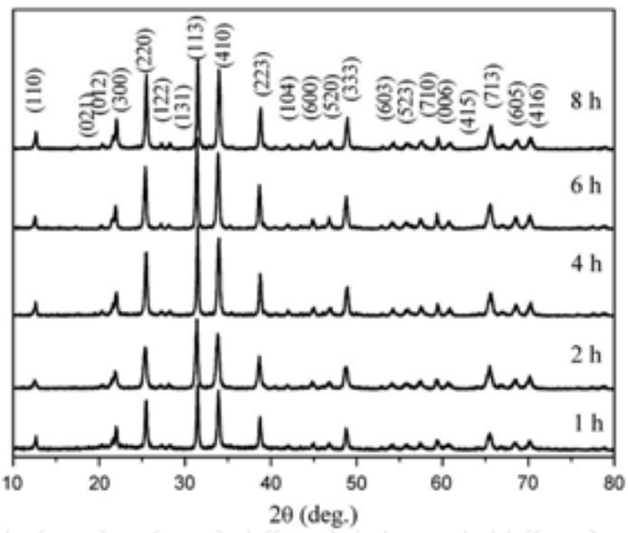

Fig. 21. XRD patterns of the Zn_2SiO_4:Mn^{2+} samples heated for different time.

When CTAB as the surfactant molecules was added in the hydrothermal procedure, it was found that the size and the morphology of the Zn_2SiO_4:Mn^{2+} phosphors could be controlled as shown in Fig. 22 a-d. When the CTAB/TEOS=0.01 was adopted, the rod-like particles show the trends to the sphere-like shaped (Fig. 22b). This is an interim morphology from rod-like to spheres. When the concentration of CTAB increased to CTAB/TEOS=0.05, TEM micrograph (Fig. 22c) shows that the willemite phosphors are nano-spheres with the diameter about 60 nm. The nanoparticles dispersed well without agglomerated. When larger amount of CTAB are introduced, nanoparticles aggregates can be observed in the final products. It was known that the surfactant molecules could adsorb on the surface of particles and stabilize the particle by either electrostatic repulsion or steric force. Therefore, the particle size and shape of Zn_2SiO_4:Mn^{2+} nanoparticles would be limited and controlled by the presence of CTAB in the hydrothermal procedure as shown in Fig. 22.

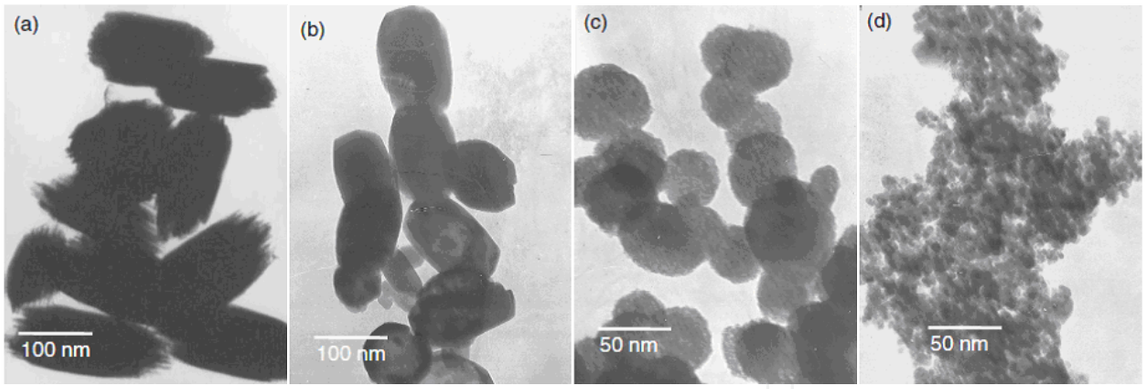

Fig. 22. TEM micrographs of the $Zn_2SiO_4:Mn^{2+}$ samples synthesized at different conditions. (a) Without CTAB, (b) CTAB/TEOS = 0.01, (c) CTAB/TEOS = 0.05, (d) CTAB/TEOS = 0.20.

The relative PL intensities of $Zn_2SiO_4:Mn^{2+}$ samples at different temperatures for different time under the 147 nm excitation are given in Fig. 23. Fig. 23a is for the samples synthesized at different temperatures for 4 hours and Fig. 23b is for the samples heated for different time at 220 °C. The strongest broad band emission at about 523 nm was observed both in Figs. 23a and b, which is attributed to the $^4T1$-$^6A1$ transition of Mn^{2+}. It shows that the luminescence intensity increase when the temperature and the time increases. We ascribe this phenomenon to the higher crystallinity according to the XRD results as discussed previously.

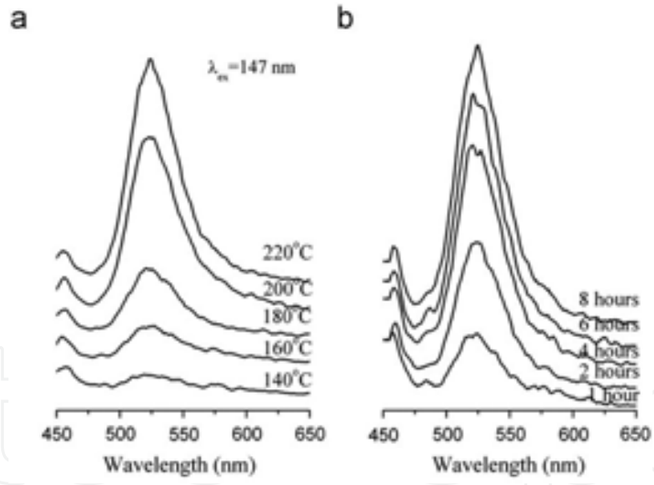

Fig. 23. Emission spectra of the $Zn_2SiO_4:Mn^{2+}$ samples under 147 excitation: (a) samples prepared at different temperatures for 4 hours and (b) samples heated for different time at 220°C.

The PL intensity among different morphology of the phosphors was also investigated. Fig. 24 presents emission spectra for the samples with different morphology under VUV excitation. The green luminescence is the conventional green of $Zn_2SiO_4:Mn^{2+}$ phosphor, occurring at about 523 nm. As can be seen in Fig. 24, the shape change of phosphors has a certain extent influence on their luminescent intensity. It can be seen that the highest PL intensity was obtained when the $Zn_2SiO_4:Mn^{2+}$ phosphor has uniform spherical morphology (sample c) due to the unique properties of sphere morphology.

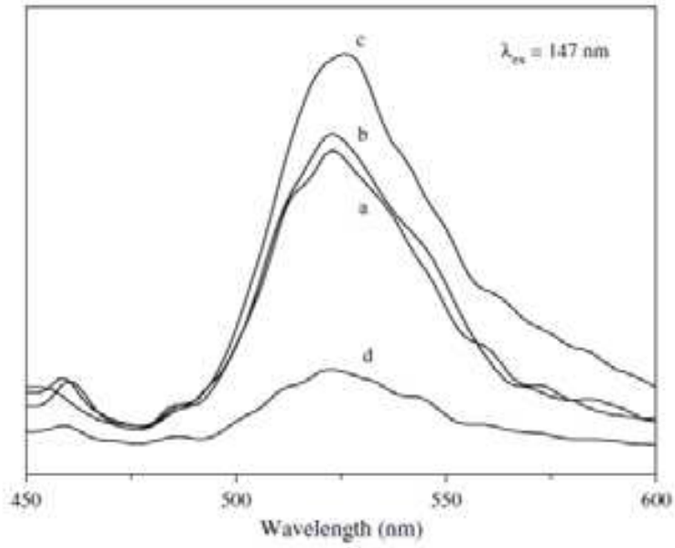

Fig. 24. Emission spectra of the $Zn_2SiO_4:Mn^{2+}$ samples: (a) without CTAB, (b) CTAB/TEOS = 0.01, (c) CTAB/TEOS = 0.05, (d) CTAB/TEOS = 0.20.

3.2 Improved PL properties of $Zn_2SiO_4:Mn^{2+}$ nanophosphors

To improve the luminescence intensity of $Zn_2SiO_4:Mn^{2+}$ nanophosphors, we carried out a heat treatment to the hydrothermally prepared spherical sample. Fig. 25 is the XRD patterns of the samples heat treated at different temperature. The relative diffraction intensity increased when the heat-treatment temperature increased, which indicated that the crystallinity of phosphor is improved by heat treatment.

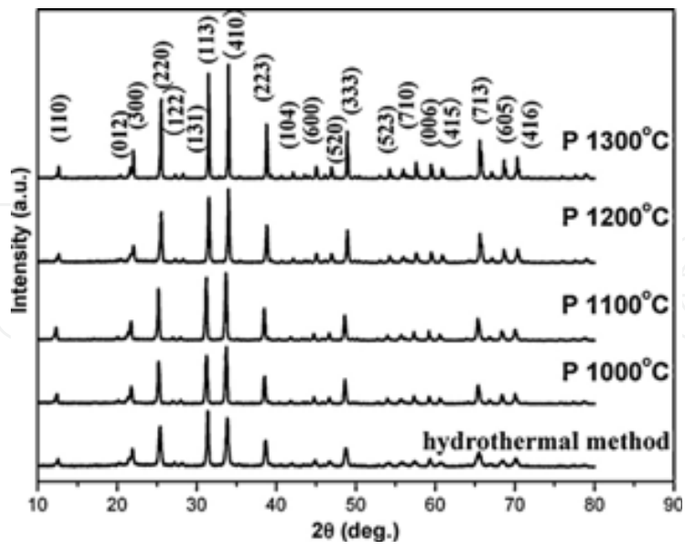

Fig. 25. XRD patterns of the $Zn_2SiO_4:Mn^{2+}$ samples post treatment at different temperature.

Fig. 26 is the TEM micrograph and size histograms of the Zn_2SiO_4: Mn^{2+} samples derived from hydrothermal method and post heat treated at 1300°C, Fig. 26a is the TEM micrograph of a typical morphology of $Zn_2SiO_4:Mn^{2+}$ samples derived from hydrothermal method. It can be

seen that the $Zn_2SiO_4:Mn^{2+}$ nanophosphors have spherical and uniform morphology. After post heat treated at 1300°C, these $Zn_2SiO_4:Mn^{2+}$ nanophosphors keep the spherical shape, fine particle size and monodispersed characteristics as shown in Fig. 26b. Fig. 26c and d are the size histograms of specimens estimating the longest dimension for over 100 particles of samples shown in Fig. 26a and b. The mean diameter is 55±25% and 85±15% nm of these samples, respectively. As a conclusion, spherical $Zn_2SiO_4:Mn^{2+}$ nanophosphor with monodispersed morphology could be synthesized by this hydrothermal and post treatment process.

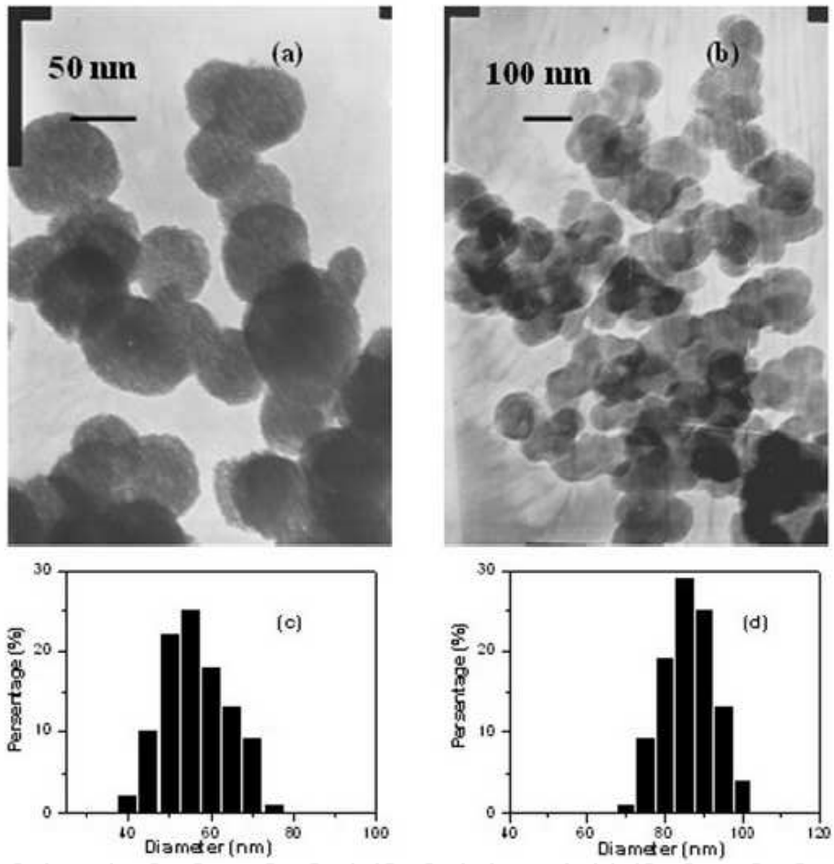

Fig. 26. TEM graphs of $Zn_2SiO_4:Mn^{2+}$ nanophosphor samples derived from hydrothermal method (a) and post heat treated at 1300°C (b). Size histograms of $Zn_2SiO_4:Mn^{2+}$ nanophosphor samples derived from hydrothermal method (c) and post heat treated at 1300°C (d).

Fig. 27 shows the relative PL intensity of $Zn_2SiO_4:Mn^{2+}$ nanophosphors after post treatment under the 147nm excitation. As can be seen in Fig. 27, the luminescence intensity about 525nm increases when the heat-treatment temperature increases, which could be ascribed to the improved crystallinity as seen in XRD section. The $Zn_2SiO_4:Mn^{2+}$ nanophosphors post heat treated at 1300°C has the maximum PL intensity, which is 86% of the commercial bulk phosphor (KX-502). Additionally, compared with commercial phosphor, PL peak of our samples located at the shorter wavelength. Because the energy band structure in nanoparticles is different from that of commercial bulk phosphor, the broadened energy gap

in nanoscale phosphor[57] result in the emission peaks of Mn^{2+} blue shift (4 nm) compared with commercial bulk phosphor.

Fig. 28 shows the decay curves of $Zn_2SiO_4:Mn^{2+}$ nanophosphors post treatment at different temperatures. The mean decay time ($\tau_{1/e}$) of the $Zn_2SiO_4:Mn^{2+}$ nanophosphor is elongated from 6.248 to 9.451ms conspicuously when the heat-treatment temperature increased from 1100 °C to 1300 °C. However, the decay time of $Zn_2SiO_4:Mn^{2+}$ particles after post treatment is longer than the commercial product 5.221 ms.

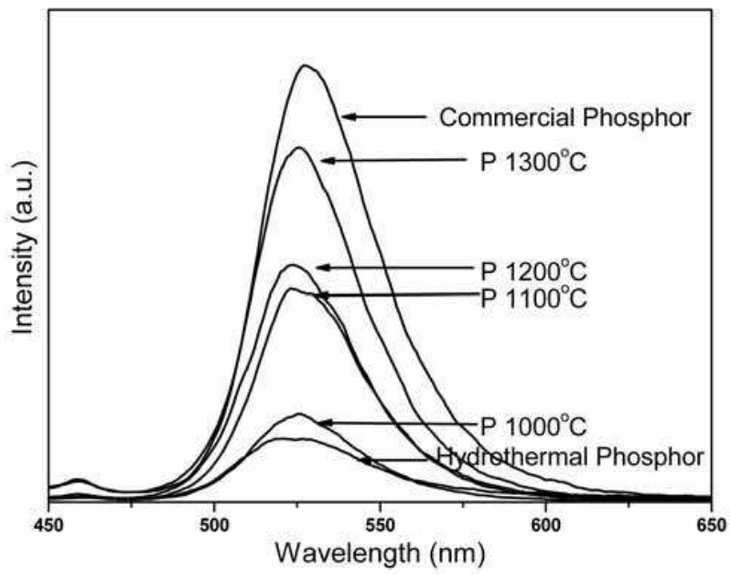

Fig. 27. Emission spectra of $Zn_2SiO_4:Mn^{2+}$ nanophosphor post treated at different temperatures and commercial phosphor

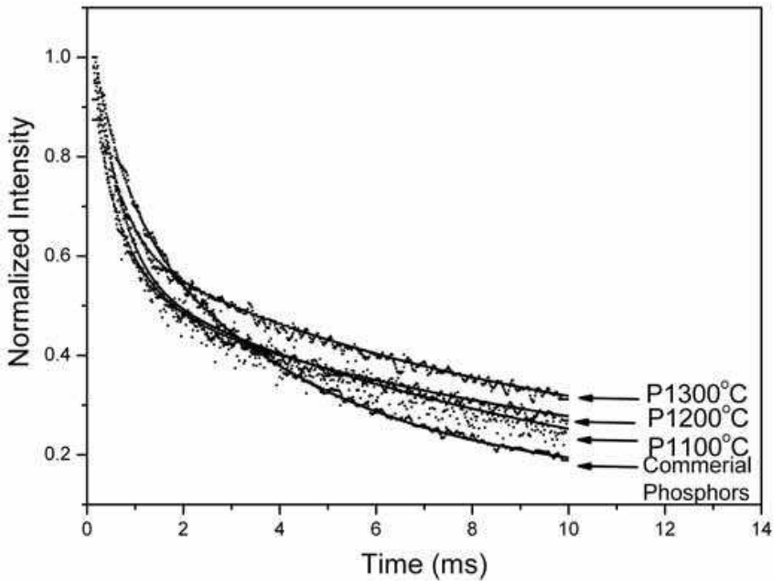

Fig. 28. Decay curves of $Zn_2SiO_4:Mn^{2+}$ nanophosphor post treated at different temperatures.

Some dopants such as Mg^{2+}, Ba^{2+}, Pb^{2+}, Li^{+}/Al^{3+} or Ga^{3+} are found to affect the decay and efficiency of Mn^{2+} in some degree when substituted for Zn^{2+} or Si^{4+} sites in bulk Zn2SiO4:Mn^{2+} phosphor.[58-62] To optimize the PL properties of Zn_2SiO_4:Mn^{2+} nanophosphors, Mg^{2+}, Ca^{2+}, Sr^{2+} and Ba^{2+} are co-doped. Fig. 29 shows XRD patterns of co-doped Zn_2SiO_4:Mn^{2+}, A^{2+} (A =Mg, Ca, Sr or Ba) nanophosphors. As shown in Fig. 29, no obvious impurity phase can be detected. Doping A^{2+} in the Zn_2SiO_4 lattice causes the diffraction peaks shift to lower 2θ positions. The changes of lattice parameter and the unit cell volume of the co-doped Zn_2SiO_4:Mn^{2+}, A^{2+} nanophosphors are shown in Tab. 6. It is clear that when A^{2+} are co-doped, both the lattice parameter and unit cell volume increase with the increased ionic radius of the A^{2+}, which attribute to substitution of A^{2+} for Zn^{2+}.

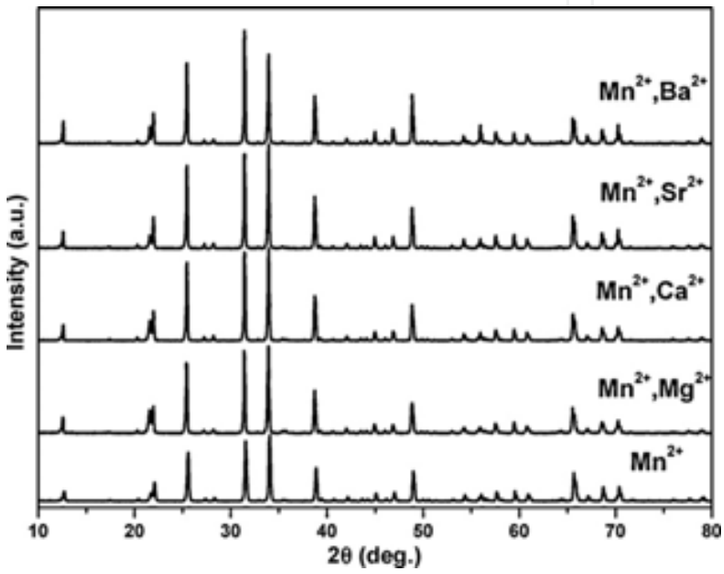

Fig. 29. XRD patterns of the Zn_2SiO_4:Mn^{2+} samples co-doped with Mg^{2+}, Ca^{2+}, Sr^{2+} or Ba^{2+} ions.

Zn_2SiO_4: Mn^{2+}, A^{2+}	Lattice parameter (nm)		Unit cell volume (nm^3)
	a	c	
Zn_2SiO_4: Mn^{2+}	1.3928(6)	0.9310(5)	1.56433
Zn_2SiO_4: Mn^{2+},Mg^{2+}	1.3932(4)	0.9321(9)	1.57031
Zn_2SiO_4: Mn^{2+},Ca^{2+}	1.3954(0)	0.9322(8)	1.57200
Zn_2SiO_4: Mn^{2+}, Sr^{2+}	1.3955(1)	0.9326(0)	1.57286
Zn_2SiO_4: Mn^{2+}, Ba^{2+}	1.3955(2)	0.9327(9)	1.57290

Table 6. Lattice parameter and unit cell volume of Zn_2SiO_4:Mn^{2+}, A^{2+}.

The influence of the co-doped A^{2+} on the PL properties of Zn_2SiO_4:Mn^{2+} nanophosphors is shown in Fig. 30. Under 147nm excitation, the PL intensity of Zn_2SiO_4:Mn^{2+} , A^{2+} (A =Mg, Ca, Sr or Ba) nanophosphors exhibit green emission which has been assigned to an electronic transition of $^4T1$ (4G)→$^6A1$ (6S) peaking around the wavelength 525nm and which is a spin and parity forbidden emission transition of Mn^{2+}. The PL intensity of Zn_2SiO_4:Mn^{2+}, A^{2+} (A =Mg, Ca, Sr or Ba) is obviously superior to that of non-codoped samples. Among these samples, the optimum PL intensity of Zn_2SiO_4:Mn^{2+}, Ca^{2+} is 107% of that of

commercial phosphors. This indicates that the co-doped ions do affect radiative transition probabilities and energy transfer characteristics between excited Mn^{2+}. The co-doped ions of A^{2+} give rise to lattice parameter increased and Zn_2SiO_4 crystal lattice expansion. This distortion of Zn_2SiO_4 lattice results in the double forbidden transition of $^4T1$ (4G)→$^6A1$ (6S) of Mn^{2+} relieved to some extent, then the emission of Mn^{2+} could be improved as shown in Fig. 30. Fig. 31 shows the decay curves of Zn_2SiO_4:Mn^{2+}, A^{2+} (A =Mg, Ca, Sr or Ba) nanophosphor and commercial phosphor under 147nm excitation. The decay time of Mg^{2+} co-doped Zn_2SiO_4:Mn^{2+} is 4.981 ms, which is much shorter than the commercial bulk phosphor. This decay time could be favorable for PDP application. However, Ca^{2+}, Sr^{2+}, Ba^{2+} co-doped samples have much longer decay time, 6.378 ms, 6.472ms and 7.529 ms, respectively. The inset of Fig. 31 exhibits the relative intensity and decay time of codoped samples summarily. Both the relative PL intensity and the decay time of Zn_2SiO_4:Mn^{2+} improved by the co-doping of A^{2+}.

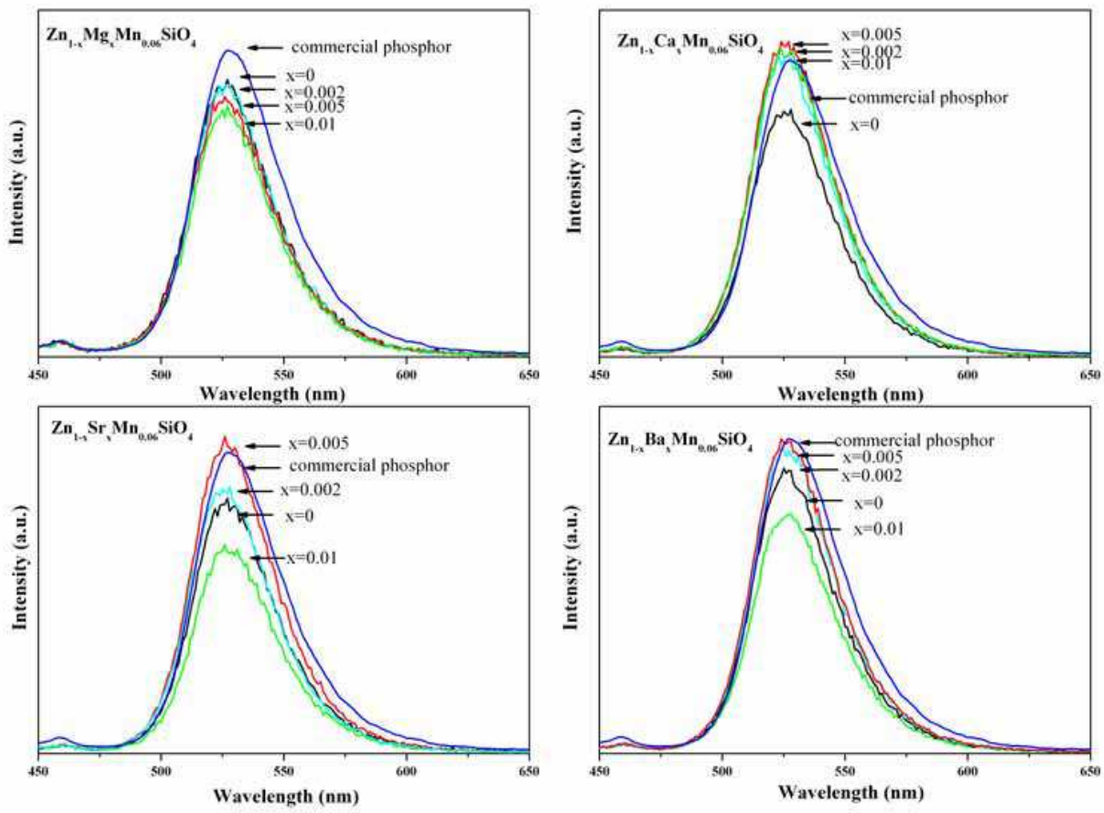

Fig. 30. Emission spectra of Zn_2SiO_4:Mn^{2+}, A^{2+} (A = Mg, Ca, Sr, Ba) nanophosphor under 147nm excitation.

3.3 Unique PL properties of Zn_2SiO_4: Mn^{2+} nanophosphors

We could control the particle sizes of the uniform Zn_2SiO_4:Mn^{2+} nanophosphors via the hydrothermal method by adjusting the surfactant amount and the hydrothermal temperature as shown in Fig. 32. Interesting finding is that with the decrease of particle size, the concentration quenching occurs at different Mn^{2+} concentration exhibited in Fig. 33.

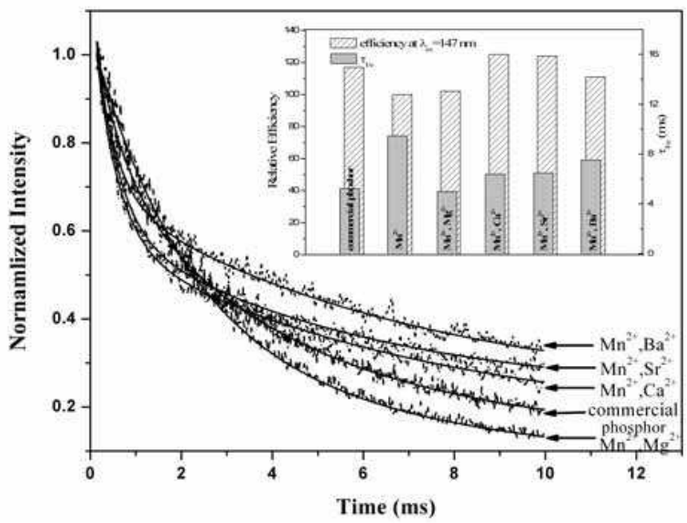

Fig. 31. Decay curves of $Zn_2SiO_4:Mn^{2+}$, A^{2+} (A =Mg, Ca, Sr, Ba) nanophosphor at 147nm excitation. Inset, efficiency and decay time of $Zn_2SiO_4:Mn^{2+}$, A^{2+} (A=Mg, Ca, Sr, Ba) nanophosphor and commercial phosphor.

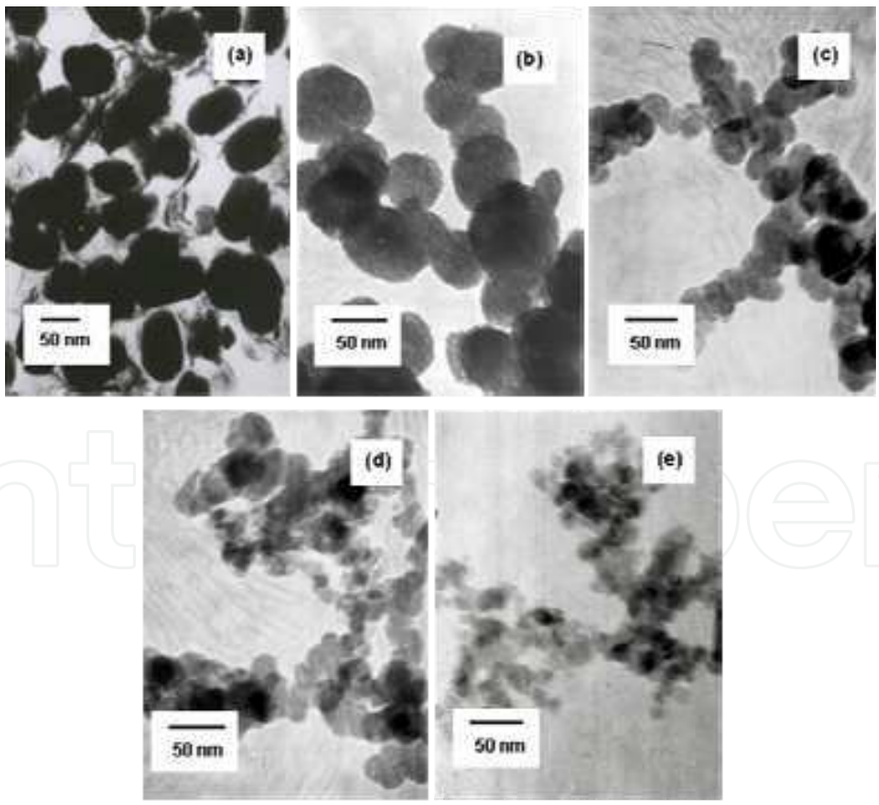

Fig. 32. TEM micrographs of the $Zn_2SiO_4:Mn^{2+}$ samples synthesized at different hydrothermal conditions. (a) ×CTAB, (b) ×2CTAB, (c) ×3CTAB at hydrothermal temperature 220°C. (d) ×3CTAB at hydrothermal temperature 180°C, (e) ×3CTAB at hydrothermal temperature 140°C.

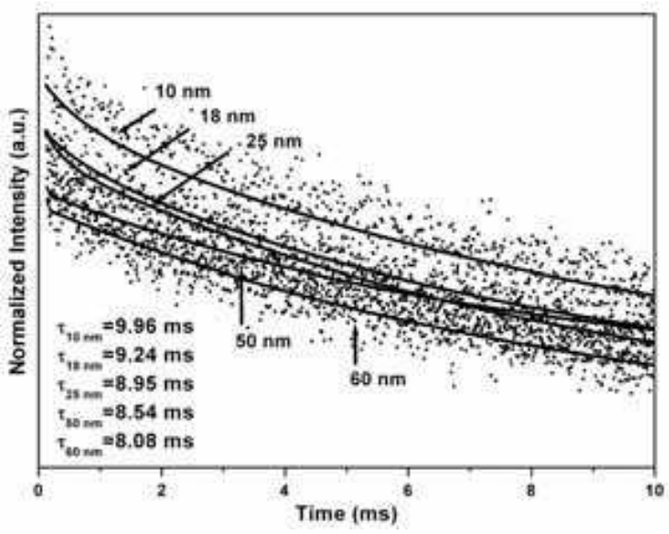

Fig. 33. Emission spectra of $Zn_{2-x}SiO_4$: xMn nanophosphors with different particle sizes under 147 nm excitation.

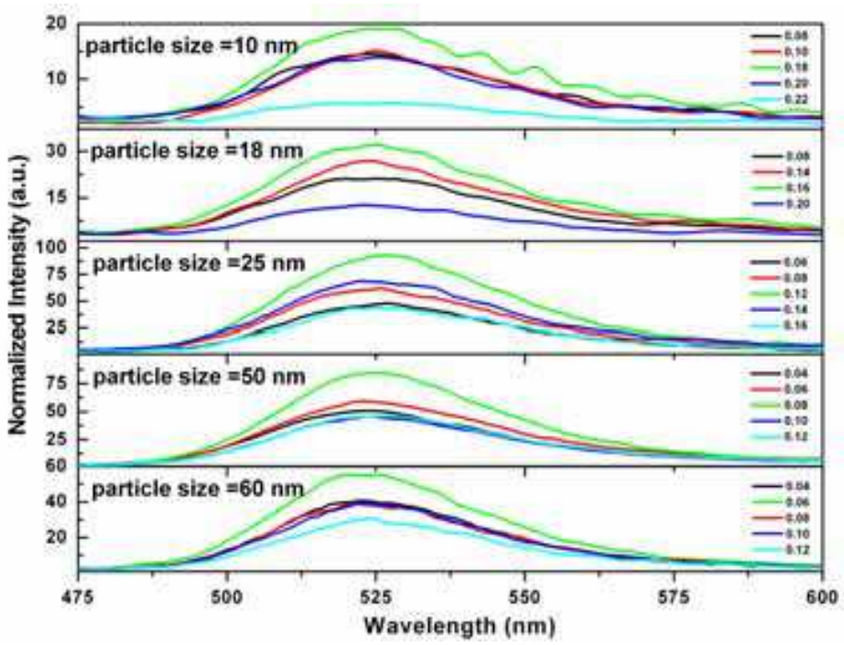

Fig. 34. Normalized decay curves of $Zn_{2-x}SiO_4$: xMn (x=0.12) nanophosphors with different particle sizes.

In $Zn_{2-x}Mn_xSiO_4$ of 60 nm, when x= 0.06, the sample shows strongest PL emission, while when the particle size decreased to 10 nm, it occurs at x=0.18. As we know, when the rate of nonradiative transitions surpassed that of radiative ones, the concentration quenching occurs. Because there existed quantities of grain boundaries in nanosized particles, which made the energy of excitation confined in almost "isolated" unit of Mn^{2+}, that is, the rate of nonradiative transitions was suppressed for the resonant energy transfer between Mn^{2+} ions. Therefore, the concentration of quenching in the Zn_2SiO_4:Mn^{2+} nanophosphors increased when the particles

decreased. Decay time of $Zn_2SiO_4:Mn^{2+}$ nanophosphor prolonged with decrease particle sizes due to the exchange interaction between Mn^{2+} ions decreased as shown in Fig. 34. These results indicate that particle sizes of nanophosphors played an important role in the changes of photoluminescence properties of $Zn_2SiO_4:Mn^{2+}$ under vuv excitation.

4. Blue phosphor of $BaMgAl_{10}O_{17}:Eu^{2+}$

$BaMgAl_{10}O_{17}:Eu^{2+}$ (BAM), as an efficient blue-emission phosphor, has been widely used in PDPs, FEDs, and fluorescence lamps (FLs).[63,64] BAM phosphors are usually prepared by the solid-state reaction. In this process, high-temperature heating is necessary, and the phosphors have a large size range and irregular shapes. It is reported that an increase in temperature leads to an increased particle size and surface morphology.[65] As nano-phosphors have small size effect, surface effect, and the quantum size effect, they present different optical and electrical properties.[66] Besides, for the application, nano-phosphors are easy to brush screen and get higher resolution to make the pictures more vivid. Thus, it is necessary to obtain nanosized BAM phosphors with low reaction temperature. As sol-gel method is an efficient technique for preparation of nanosized materials, we adopt it to synthesize BAM nanophosphor and investigate the photoluminescence in VUV region.

4.1 Controllable morphology of BAM nanophosphors

Fig. 35 shows the typical XRD patterns of the $BaMgAl_{10}O_{17}:Eu^{2+}$ samples by sol-gel method under different temperatures for 4 h. At 850°C, the sample was amorphous. When the temperature rose to 1,200°C, the BAM phase began to form but still had an impurity peak ($BaAl_2O_4$). When the temperature increased to 1,250°C, the impurity peak disappeared and formed a good BAM phase. It matched well with the JCPDF (26-0163) files of BAM. After further improve the reaction temperature to 1300°C, the crystalline was also single-phase and the crystallinity was much enhanced. On the contrary to this technique, in conventional solid-state reaction, the presence of intermediates was identified which brought on impurities in the product even at the temperature of 1600°C.[67]

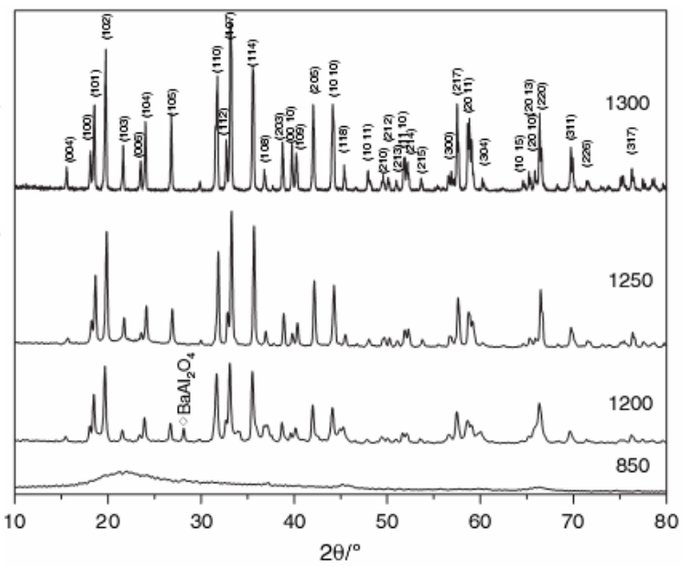

Fig. 35. XRD patterns for $BaMgAl_{10}O_{17}:Eu^{2+}$ at different temperatures.

Fig. 36 exhibits the SEM micrographs of the BAM samples under 1250°C (a) and 1300°C (b). As $BaMgAl_{10}O_{17}$ has the crystal structure of β-alumina, the particle takes the form of hexagonal platelets when the crystal freely grows,[68] but from the images, the nanorods can be obviously seen and have a homogeneous grain size at 80–100 nm in diameter and 0.8–1 μm in length. This morphology is different from that of samples synthesized by other methods that result in irregular morphology, such as the solid-state method,[69] oxalate co-precipitation process,[70,71] and microwave irradiation synthesis methods.[72] The advantages of sol-gel method could be responsible for this phenomenon, such as good mixing of starting materials in molecular level, limiting reaction space and relatively low reaction temperature.[73]

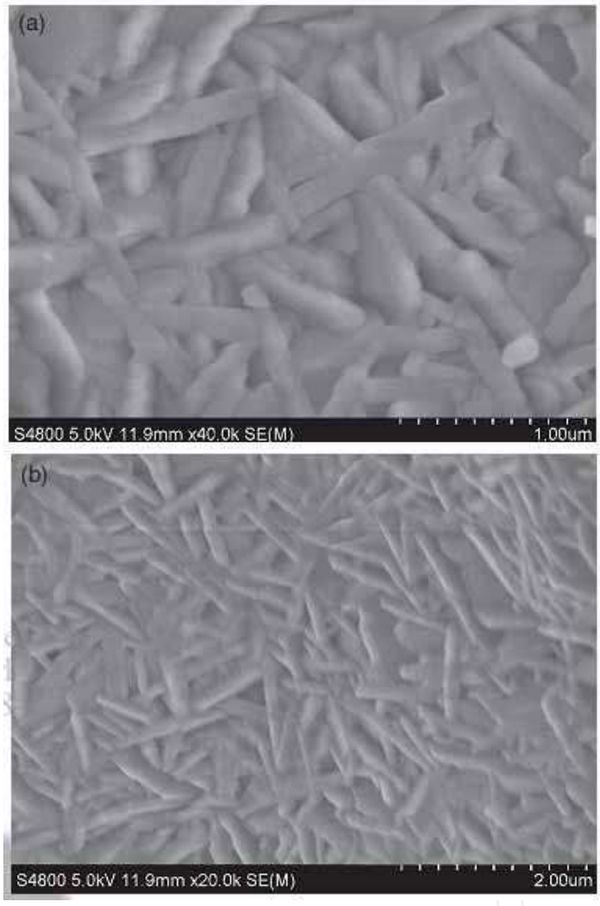

Fig. 36. SEM images of BAM phosphors synthesized at (a) 1250°C and (b) 1300°C.

It has been reported in the systems of ZnO and $ZnSiO_4$: Mn that the addition of cetyl-tri-methyl-ammonium bromide (CTAB) in sol-gel process could improve their luminescent intensity attributing to the interaction between CTA^+ and anionic group.[14,74,75] Fig. 37 shows the typical XRD patterns of the $BaMgAl_{10}O_{17}:Eu^{2+}$ phosphors synthesized at 1300°C with different concentration of CTAB. All of the peaks can be indexed and they match well with JCPDF (26-0163) file of BAM. The result indicates the phosphor obtained by sol-gel process is monophasic BAM ascribing to the well disperse of the precursor powder.

To investigate the effect of CTAB on the morphology of BAM crystalline, the SEM images of the samples with adding CTAB is investigated in Fig. 38. From the micrographs, the sample

derived from CTAB assisted sol-gel process exhibits the morphology of nanosheets with about 100nm in thickness. It shows that the morphology of BAM derived from sol-gel method can be altered by the addition of surfactant CTAB. As $BaMgAl_{10}O_{17}$ has the crystal structure of β-alumina, the particle conventionally takes the form of hexagonal platelets when the crystal freely grows. The different morphologies in this work and the phenomenon of the alteration from rods to sheets (as shown in Fig. 36 and Fig. 38) could be explained by the BAM crystal growth mechanisms of different procedures.

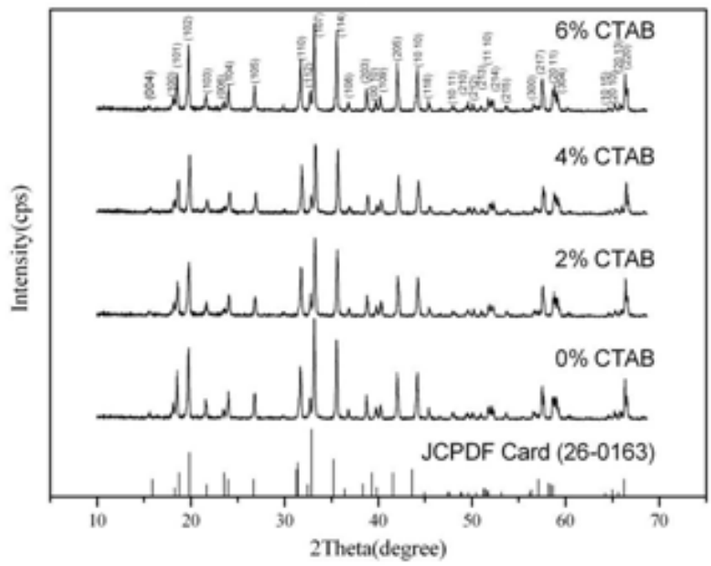

Fig. 37. Typical XRD patterns of the $BaMgAl_{10}O_{17}:Eu^{2+}$ phosphors synthesized at 1300°C with different concentration of CTAB.

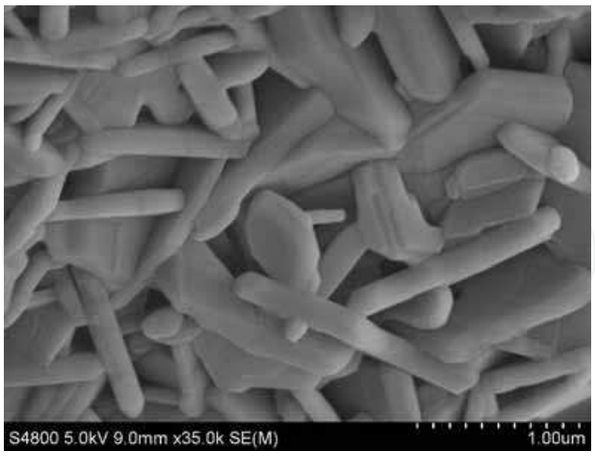

Fig. 38. SEM image of the sample synthesized with adding CTAB.

The crystal growth mechanisms of BAM derived from sol-gel process can be illustrated in Fig. 39. Fig. 39a depicts the formation process of BAM nano-rods, and Fig. 39b presents the mechanisms of the formation of nano-sheets while CTAB is added. In the route (a), first, all metal ions in the initial solution are in hydration state, which reject with the hydrogen ions in the water leading to a series of hydrolysis reactions (as shown in equation 1). After the

metal ions hydrolyzing in the form of precipitation, it could be dissolved with the adding of citric acid, which is called precipitation-peptization reaction (as shown in equation 2). In these reactions, the colloid seeds are produced, which is positive charge covering with anions of equal charge.

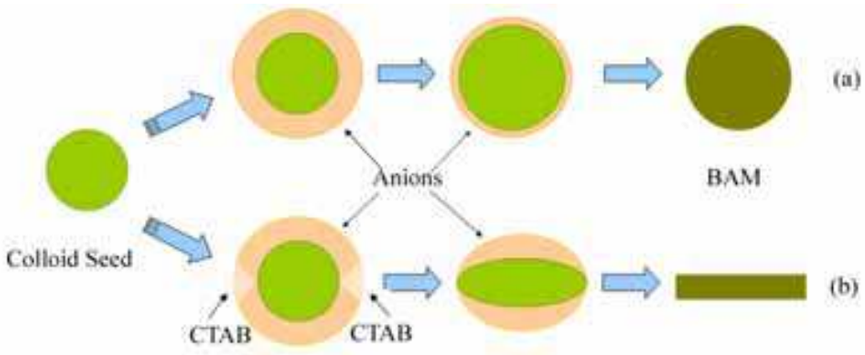

Fig. 39. Possible formation processes of BAM nano-rods, and nano-sheets.

$$M(H_2O)_x{}^{z+} = M(H_2O)_{x-1}(OH)^{(z-1)} + H^+ \text{ ------ } M(OH)_n \quad (1)$$

$$a\,[M(OH)_n\,(H_2O)_x]^0 + b\,C_6H_8O_7 = \{[M(OH)_n(H_2O)_x]_aH_b\}^{b+} + bC_6H_7O_7^- \quad (2)$$

The colloid seeds in this process are $\{[M(OH)_n(H_2O)_x]_aH_b\}^{b+}$ covered by $C_6H_7O_7^-$ due to the Coulomb's force. Therefore, the reaction of the formation of BAM phase is limited in the space. By calcination, the anions on the surface could be decomposed into CO_2 and H_2O and BAM nano-rods could be produced via calcination (as shown in Fig. 36 (a)). It has been known that the adsorption of units on crystal surfaces strongly affects the growth speed and orientation of crystals.[69,76] When cationic surfactant CTAB is introduced in this process, the positive charge CTA^+ ion could carry the anions on the surface of the colloid seeds by electrostatic interaction, which makes the BAM crystalline grow in the direction of absent anions when calcined (as shown in Fig. 38 (b)). This difference could be responsible for the alternation of the morphology from rods to sheets. by calcination and forms the morphology of sheets (as shown in Fig. 38).

4.2 Improvement PL performance of BAM nanophosphors

Fig. 40 illustrates the comparison of the emission spectra among commercial $BaMgAl_{10}O_{17}:Eu^{2+}$ blue phosphor and nano-phosphors synthesized by the sol-gel method under 1,300 and 1,250°C by 147 nm excitation. As shown in Fig. 40, a broad emission band can be seen, and the peak is located at 452 nm. It is attributed to the $4f^65d \rightarrow 4f^7$ ($^8S_{7/2}$) transition of Eu^{2+}. With the temperature increasing from 1,250 to 1,300°C, the emission intensity of these nano-phosphors by 147 nm excited enhanced about 22%, and the intensity of the nano-phosphor synthesized by the sol-gel method at 1,300°C was 78.15% of the commercial phosphor.

From Fig. 40, the nano-phosphors have perfect photoluminescence properties. As Maas *et al.*[33] reported that phosphors prepared by the wet chemical method had poor photoluminescence, this high intensity may be due to the increased specific surface area when nano-size phosphors are prepared and the relatively high synthesized temperature—compared with the hydrothermal method—at which the residual organic ions can be removed.

The photoluminescence intensity of the samples was strongly affected by the doping concentration of Eu^{2+}. To investigate the optimum Eu^{2+} concentration in this process, the relative emission intensity dependence of $Ba_{1-x}MgAl_{10}O_{17}:xEu^{2+}$ excited by 147 nm was evaluated. Fig. 41 exhibits the emission spectra of $Ba_{1-x}MgAl_{10}O_{17}:xEu^{2+}$ ($0.06 \leq x \leq 0.14$) synthesized by the sol-gel method at 1,300°C (λ_{ex} = 147 nm). The result indicates that the most intense band is observed at a content of x = 0.1 and the intensity decreases in $Ba_{1-x}MgAl_{10}O_{17}:xEu^{2+}$ (x = 0.06, 0.08, 0.12, 0.14), which is called the concentration quenching phenomenon.[77] The same phenomenon occurred when excited by 254 nm. Therefore, the optimum chemical composition is $Ba_{0.9}$ $MgAl_{10}O_{17}:0.1Eu^{2+}$ in the sol-gel process.

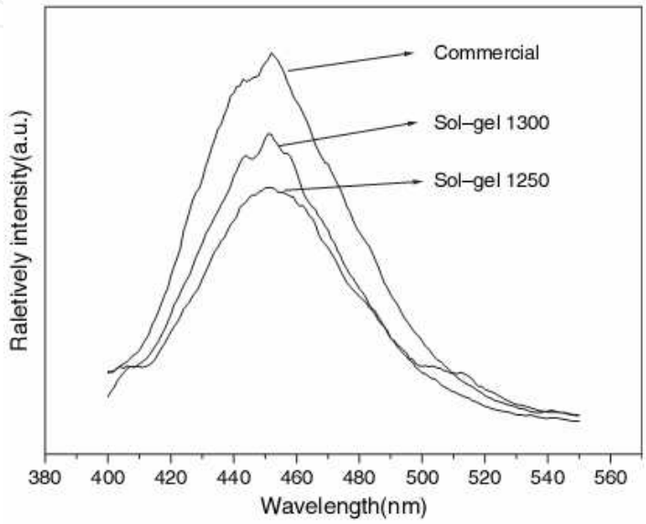

Fig. 40. Emission spectra of commercial $BaMgAl_{10}O_{17}:Eu^{2+}$ blue phosphor and nano-phosphors synthesized by sol-gel method under 1,300°C and 1,250°C (λ_{ex} = 147 nm)

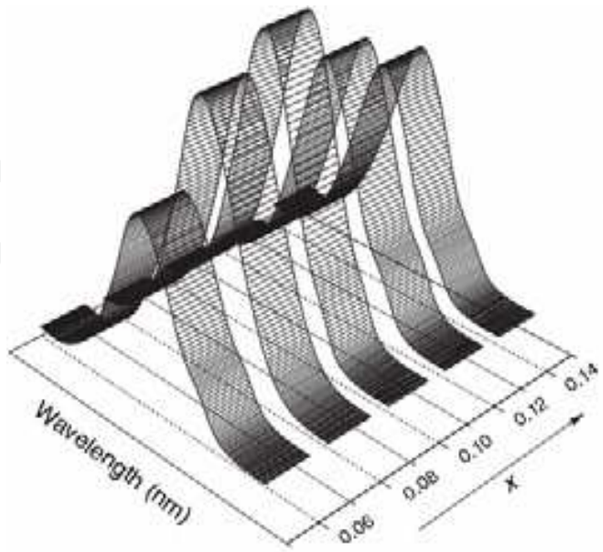

Fig. 41. Emission spectra of $Ba_{1-x}MgAl_{10}O_{17}:xEu^{2+}$ ($0.06 \leq x \leq 0.14$) synthesized by sol-gel method at 1300°C (λ_{ex} = 147 nm)

The color coordinates of commercial $BaMgAl_{10}O_{17}:Eu^{2+}$ blue phosphor and nano-phosphors synthesized by the sol-gel method under 1,300°C and 1,250°C by 147 nm and 254 nm excitation are exhibited in Tab. 7. It can be found that the y value in color coordinates of the samples prepared by the sol-gel process is much lower than that of standard blue fluorescence. These low y values indicate that the nanophosphor is useful for restricting the decrease of BAM effciency during heating and the fitting y value should between 0.06 and 0.1.[78,79]

Samples	Coordinates (λ_{ex} =147nm)	Coordinates (λ_{ex} =254nm)
Commercial phosphor	(0.144, 0.069)	(0.144, 0.068)
Sol-gel 1250°C	(0.145, 0.063)	(0.144, 0.065)
Sol-gel 1,300°C	(0.143, 0.068)	(0.145, 0.062)
NTSC, blue	(0.14, 0.08)	

Table 7. The color coordinates of samples under UV and VUV excitation

However, the luminescence intensity and thermal stability of the BAM nanorods in VUV region still could not meet the requirement of the commercial use. Futher improvements on the nanorods are necessary. In the systems of ZnO and $ZnSiO_4$: Mn, it was found that the addition of cetyl-tri-methyl-ammonium bromide (CTAB) in sol-gel process could improve their luminescent intensity attributing to the interaction between CTA^+ and anionic group.[14,74,75] Moreover, the doping of Mg^{2+} to substitute Al^{3+} in the bulk BAM could effectively restrain the thermal degradation.[80] Hence Mg^{2+} and CTAB were introduced in sol-gel method for synthesizing BAM nanophosphor.

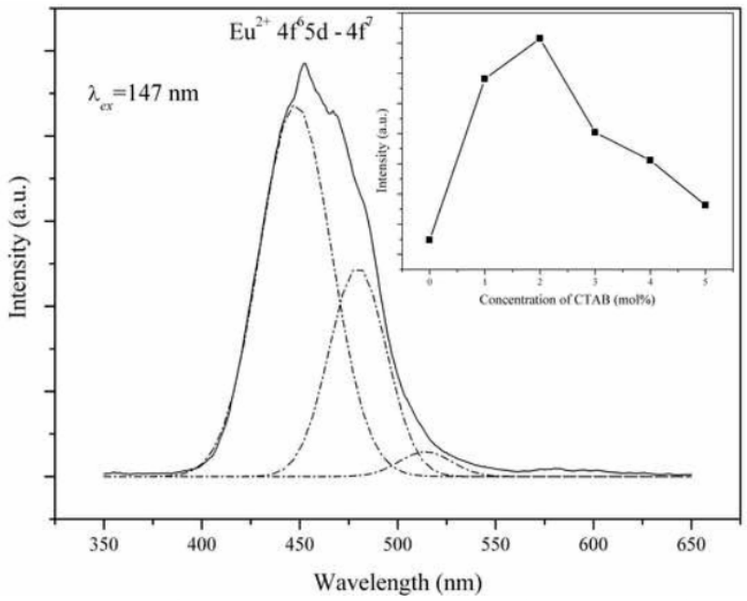

Fig. 42. Emission spectrum of BAM nanorods doped with 2% CTAB by 147 nm excitation (solid line); The dashed line exhibits the Gaussian fitting result of the spectrum; The inset is the relative emission intensity of the nanophosphors with different concentration of CTAB.

Fig. 42 shows the emission spectrum of BAM nanorods doped with 2% CTAB (λ_{ex} = 147 nm). The emission spectrum presents a broad band locating at about 452 nm, which attributes to the $4f^65d \rightarrow 4f^7(^8S_{7/2})$ transition of Eu^{2+}. The band is of asymmetrical distribution which relates to the different sites that Eu^{2+} occupy in BAM. By Gaussian fitting the VUV emission spectrum, three peaks are found locating at 446nm, 477nm and 517nm, respectively, corresponding to the emission of Eu^{2+} in the sites of BR, a-BR and spinel layer.[81-83] To probe into the influence of CTAB on VUV emission intensity, the luminescent properties of the nanorods with different concentration of CTAB are depicted under 147 nm excitation. From the inset of Fig. 43, it can be seen that the addition of CTAB evidently enhances the relative intensity of the nanophosphor. The optimum concentration of CTAB is determined to be 2 %, which heightens the original emission intensity about 16%. This phenomenon could be interpreted by the inherent function of the surfactant CTAB: It could not only reduce the surface tension of solution and lower the energy to form a new phase, but also eliminate the defect states through chemical interaction between surfactants and inorganic species during the synthesis.

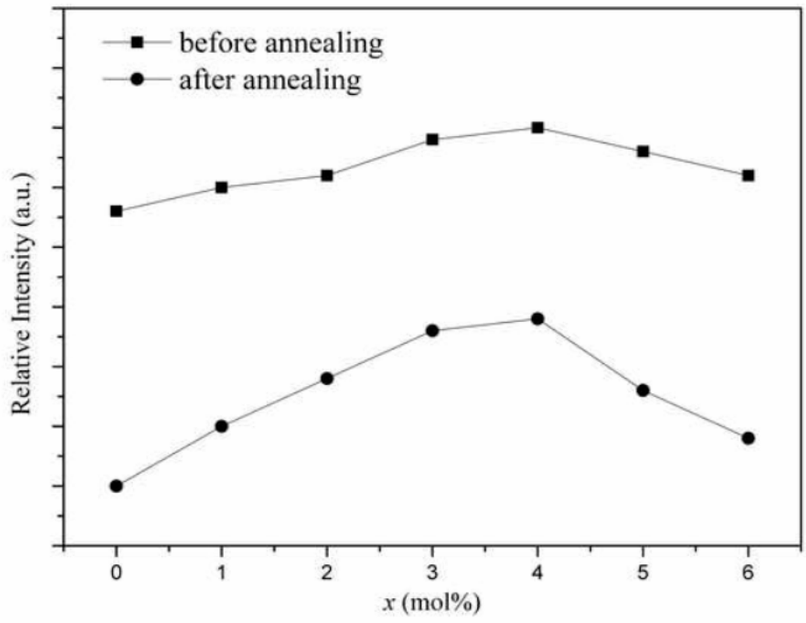

Fig. 43. Relative emission intensity of $Ba_{0.9}Mg(Al_{1-x}Mg_x)_{10}O_{17-5x}$: $0.1Eu^{2+}$ ($0 \le x \le 0.06$) nanophosphors synthesized by 2% CTAB assisted sol-gel technique before and after annealing (λ_{ex} = 147 nm).

As we know, the blue phosphor BAM could be jeopardized by the thermal degradation when heated at about 550 ^oC. The relative emission intensity of the above CTAB-prepared nanorods is valued after a heat-treatment of 550 ^oC for 1 h in air condition. Their deterioration ratios are 25.3% (0% CTAB), 24.4% (2% CTAB), 24.9% (4% CTAB) and 25.5% (6% CTAB), respectively. So the addition of CTAB in the sol-gel process does not affect the thermal stability of the BAM nanorods.

For the purpose of getting BAM nanophosphor with high emission intensity and good thermal stability, Mg^{2+} was introduced in the host on the basis of adding 2% CTAB. Fig. 43

presents the relative emission intensity of BAM nanophosphors with the variation of doping Mg^{2+} before and after annealing (λ_{ex} = 147 nm). It can be obviously found that the additional of Mg^{2+} in the sites of Al^{3+} could further enhance the emission intensity of BAM nanophosphor before and after annealing. The optimum concentration of Mg^{2+} is 4%. On one hand, due to Mg-O has absorption in VUV region, the doping of additional Mg^{2+} could enhance the emission intensity of BAM phosphor. On the other hand, since the substitution of Mg^{2+} for Al^{3+} is a substitution of lower valence cations for higher valence cations, considering the charge compensating mechanism, anion vacancies or interstitial cations must be generated in the beta alumina structure; These defects play roles on the quenching centers and decrease the emission intensity. As a result, the optimum doping concentration of Mg^{2+} is affected by the above two reasons. The thermal degradation of the optimum nanophosphor (with the addition of 2% CTAB and 4% Mg) is calculated to be 18.5%, which may be compared to a value of 6% with a nanophosphor synthesized with only 2% CTAB.

To analyze the improvement of the thermal stability, the changes of full-width at half-maximum (FWHM) and y value of color coordinates of the samples synthesized with 2% CTAB and different concentrations of Mg^{2+} are shown in Fig. 44. As mentioned in Fig. 45a, the emission spectrum of BAM is composed of three emission bands which correspond to Eu^{2+} in different sites of Ba^{2+}. With the variation of the distribution of Eu^{2+} in the three sites, the color coordinates and FWHM could change synchronously. As a result, the variations in Fig. 44 reflect the lattice environment of Eu^{2+} is changed by doping Mg^{2+}. The *y* value of the emissions for Eu^{2+} in three sites is different that it decreases with decreasing wavelength. Therefore, the decrease of *y* value with increasing the doping concentration of Mg^{2+} (as shown in Fig. 44) indicates that Eu^{2+} migrate from the sites emitting long wavelength (spinel block) to those emitting short wavelength (mirror layer). Associated with the consideration that the migration of Eu^{2+} in BAM from mirror planes to spinel blocks is another essential mechanism of the thermal degradation besides the oxidation of Eu^{2+} to Eu^{3+},[84] the introduction of Mg^{2+} to substitute Al^{3+} will certainly improve its thermal stability.

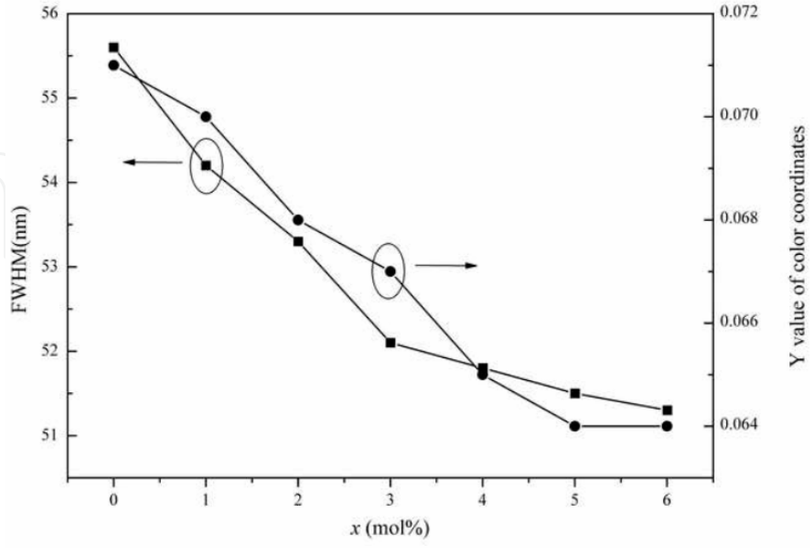

Fig. 44. FWHM and y value of color coordinates of the samples synthesized with 2% CTAB and different concentration of Mg^{2+}.

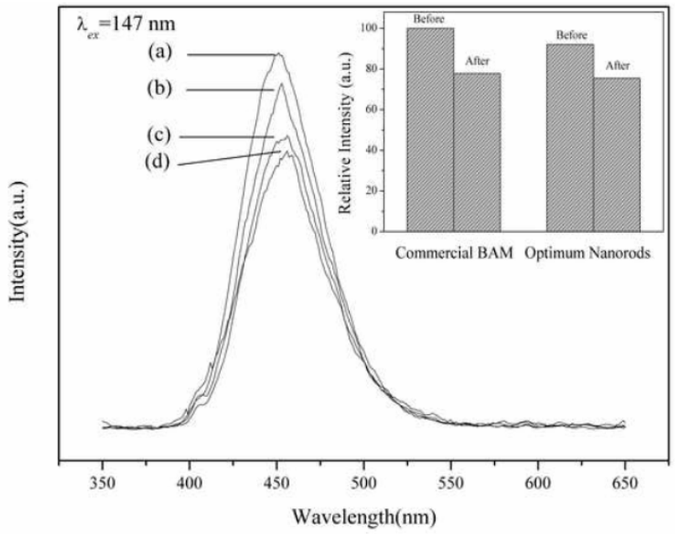

Fig. 45. Emission spectra of BAM samples: (a) commercial phosphor, before annealing, (b) optimum nanorods, before annealing, (c) commercial phosphor, after annealing, (d) optimum nanorods, after annealing (λ_{ex}=147nm); The inset is the columnar graph of the emission intensity.

Therefore, the optimum nanoscaled BAM is that synthesized by 2% CTAB assisted sol-gel method with 4% Mg^{2+} doped. The comparison between the optimum nanorods and commercial BAM phosphor (kx-501) on emission intensity and thermal stability are illustrated in Fig.45 (λ_{ex} = 147 nm). Before annealing, the luminescence intensity of the nanorods is nearly 92% of that of the commercial phosphor. After annealing, the luminescence intensity of the nanorods is nearly 97% of that of the annealed commercial phosphor. These data reflect that the thermal stability of the nanorods is superior to that of the commercial phosphor, and the BAM nanorods could be potentially applied in high resolution plasma display panels.

5. Acknowledgement

This work is supported by National Natural Science Foundation of China (No. 10874061), National Science Foundation for Distinguished Young Scholars (No. 50925206) and The Research Fund for the Doctoral Program of Higher Education (No. 200807300010).

6. References

[1] Jűstel, T.; Nikol, H. *Adv. Mater.* 2000, *12*, 527.
[2] Heynderickx, I.; Langendijk, E. "Image Quality Comparison of PDP, LCD, CRT, and LCoS Projection", 2005.
[3] Lu, H.; Chen, H.; Tseng, T.; Kuo, W.; Alam, M.; Cheng, B. *J Electron Spectrosc* 2005, *144*, 983.
[4] Kim, C.; Kwon, I.; Park, C.; Hwang, Y.; Bae, H.; Yu, B.; Pyun, C.; Hong, G. *J Alloy. Compd.* 2000, *311*, 33.
[5] Wang, Y.; Uheda, K.; Takizawa, H.; Mizumoto, U.; Endo, T. *J Electrochem. Soc.* 2001, *148*, G430.
[6] Li, Z.; Zeng, J.; Li, Y. *Small* 2007, *3*, 438.
[7] Rao, R. P. *J Lumin.* 2005, *113*, 271.
[8] Zhang, H.; Fu, X.; Niu, S.; Sun, G.; Xin, Q. *J Solid State Chem.* 2004, *177*, 2649.

[9] Wu, H.; Xu, H.; Su, Q.; Chen, T.; Wu, M. *J Mater. Chem.* 2003, *13*, 1223.
[10] Wang, G.; Qin, W.; Zhang, D.; Wang, L.; Wei, G.; Zhu, P.; Kim, R. *J Phys. Chem. C* 2008, *112*, 17042.
[11] Guo, X.; Wang, Y.; Zhang, J. *J Cryst. Growth* 2009, *311*, 2409.
[12] Dong, Q.; Wang, Y. *Journal of Nanoscience and Nanotechnology* 2010, *10*, 1794.
[13] Yu, X.; Wang, Y. *Journal of Nanoscience and Nanotechnology* 2010, *10*, 2173.
[14] Yu, X.; Wang, Y. *J Phys. Chem. Solids* 2009, *70*, 1146.
[15] Yu, X.; Wang, Y. *J Alloy. Compd.* 2010.
[16] Wang, Z.; Wang, Y.; Liu, B. *Journal of Nanoscience and Nanotechnology* 2010, *10*, 2177.
[17] Wang, Z., Y. Wang, Y. Li, and B. Liu, *J Alloy. Compd.* 2011, 509, 343.
[18] Wang, Y., Z. Wang, X. Yu, and Q. Dong, International Journal of the Society of Materials Engineering for Resources 2010, 17, 93.
[19] Boyer, D., G. Bertrand-Chadeyron, R. Mahiou, C. Caperaa, and J. Cousseins, *J Mater. Chem.* 1999, 9, 211.
[20] Wei, Z., L. Sun, C. Liao, C. Yan, and S. Huang, *Appl. Phys. Lett.* 2002, 80, 1447.
[21] Wei, Z., L. Sun, C. Liao, X. Jiang, C. Yan, Y. Tao, X. Hou, and X. Ju, *J Appl. Phys.* 2003, 93, 9783.
[22] Wang, Y., K. Uheda, H. Takizawa, and T. Endo, *Chem. Lett.* 2001, 30, 206.
[23] Jiang, X., C. Yan, L. Sun, Z. Wei, and C. Liao, *J Solid State Chem.* 2003, 175, 245.
[24] Jiang, X.-C., L.-D. Sun, W. Feng, and C.-H. Yan, *Crystal Growth & Design* 2004, 4, 517.
[25] Wei, Z., L. Sun, C. Liao, X. Jiang, and C. Yan, *J Mater. Chem.* 2002, 12, 3665.
[26] Jiang, X.C., C.H. Yan, L.D. Sun, Z.G. Wei, and C.S. Liao, *J Solid State Chem.* 2003, 175, 245.
[27] Wei, Z., L. Sun, C. Liao, J. Yin, X. Jiang, and C. Yan, *J Phys. Chem. B* 2002, 106, 10610.
[28] Zhang, J. and J. Lin, *J Cryst. Growth* 2004, 271, 207.
[29] Wegh, R.T., H. Donker, K.D. Oskam, and A. Meijerink, *Science* 1999, 283, 663.
[30] Feldmann, C., T. Jüstel, C.R. Ronda, and D.U. Wiechert, *J Lumin.* 2001, 92, 245.
[31] Yin, S., Y. Aita, M. Komatsu, J. Wang, Q. Tang, and T. Sato, J. Mater. Chem. 2005, 15, 674.
[32] Yin, S., M. Shinozaki, and T. Sato, *J Lumin.* 2007, 126, 427.
[33] Maas, H., A. Currao, and G. Calzaferri, *Angewandte Chemie International Edition* 2002, 41, 2495.
[34] Terekhin, M., A. Vasil'ev, M. Kamada, E. Nakamura, and S. Kubota, *Phys. Rev. B* 1995, 52, 3117.
[35] You, H., X. Wu, X. Zeng, G. Hong, C.H. Kim, C.H. Pyun, and C.H. Park, *Materials Science and Engineering B* 2001, 86, 11.
[36] Blasse, G., *The Journal of Chemical Physics* 1966, 45, 2356.
[37] Wang, M., L. Sun, X. Fu, C. Liao, and C. Yan, *Solid State Commun.* 2000, 115, 493.
[38] Konrad, A., T. Fries, A. Gahn, F. Kummer, U. Herr, R. Tidecks, and K. Samwer, *J Appl. Phys.* 1999, 86, 3129.
[39] Ronda, C.R., T. Jüstel, and H. Nikol, *J Alloy. Compd.* 1998, 275-277, 669.
[40] Dong, Q., Y. Wang, Z. Wang, X. Yu, and B. Liu, *J Phys. Chem. C* 2010, 114, 9245.
[41] Li, Q., C. Feng, Q. Jiao, L. Guo, C. Liu, and H.B. Xu, *physica status solidi (a)* 2004, 201, 3055.
[42] Kang, Y. and H. Park, Applied Physics A: Materials Science & Processing 2003, 77, 529.
[43] Ohtake, T., K. Ohkawa, N. Sonoyama, and T. Sakata, *J Alloy. Compd.* 2006, 421, 163.
[44] Kandarakis, I., D. Cavouras, P. Prassopoulos, E. Kanellopoulos, C. Nomicos, and G. Panayiotakis, *Applied Physics A: Materials Science & Processing* 1998, 67, 521.
[45] Dinsmore, A., D. Hsu, H. Gray, S. Qadri, Y. Tian, and B. Ratna, *Appl. Phys. Lett.* 1999, 75, 802.
[46] Wang, Y., Y. Hao, and L. Yuwen, *J Alloy. Compd.* 2006, 425, 339.

[47] Roh, H., E. Kim, H. Kang, Y. Kang, H. Park, and S. Park, *Jpn. J Appl. Phys* 2003, 42, 2741.
[48] Xiong, L., J. Shi, J. Gu, L. Li, W. Huang, J. Gao, and M. Ruan, *J Phys. Chem. B* 2005, 109, 731.
[49] Patra, A., G. Baker, and S. Baker, *J Lumin.* 2005, 111, 105.
[50] Bhargava, R., D. Gallagher, X. Hong, and A. Nurmikko, *Phys. Rev. Lett.* 1994, 72, 416.
[51] Tissue, B., *Chem. Mater* 1998, 10, 2837.
[52] Zhang, H., S. Buddhudu, C. Kam, Y. Zhou, Y. Lam, K. Wong, B. Ooi, S. Ng, and W. Que, *Mater. Chem. Phys.* 2001, 68, 31.
[53] Lee, C., Y. Kang, K. Jung, and J. Choi, *Materials Science and Engineering B* 2005, 117, 210.
[54] Ahmadi, T., M. Haase, and H. Weller, *Mater. Res. Bull.* 2000, 35, 1869.
[55] Wan, J., X. Chen, Z. Wang, L. Mu, and Y. Qian, *J Cryst. Growth* 2005, 280, 239.
[56] Wang, H., Y. Ma, G. Yi, and D. Chen, *Mater. Chem. Phys.* 2003, 82, 414.
[57] Cavallini, A., L. Polenta, M. Rossi, T. Richter, M. Marso, R. Meijers, R. Calarco, and H. L¨¹th, *Nano Lett* 2006, 6, 1548.
[58] Sohn, K.-S., B. Cho, H. Chang, and H.D. Park, *J Electrochem. Soc.* 1999, 146, 2353.
[59] Wang, S., M. Lu, F. Gu, Y. Qi, D. Xu, D. Yuan, and D. Cao, *Applied Physics A: Materials Science & Processing* 2005, 80, 871.
[60] Hao, Y. and Y.-H. Wang, *J Alloy. Compd.* 2009, 470, 565.
[61] van der Kolk, E., P. Dorenbos, C.W.E. van Eijk, H. Bechtel, T. Jüstel, H. Nikol, C.R. Ronda, and D.U. Wiechert, *J Lumin.* 2000, 87-89, 1246.
[62] Hao, Y. and Y. Wang, *Electrochemical and Solid-State Letters* 2006, 9, H100.
[63] Ronda, C., *J Alloy. Compd.* 1995, 225, 534.
[64] Di, W., X. Wang, B. Chen, S. Lu, and X. Zhao, *J Phys. Chem. B* 2005, 109, 13154.
[65] Lu, C., C. Chen, and B. Bhattacharjee, *J Rare Earth.* 2006, 24, 706.
[66] Chen, W., J. Malm, V. Zwiller, Y. Huang, S. Liu, R. Wallenberg, J. Bovin, and L. Samuelson, *Phys. Rev. B* 2000, 61, 11021.
[67] Oshio, S., K. Kitamura, T. Shigeta, S. Horii, T. Matsuoka, S. Tanaka, and H. Kobayashi, *J Electrochem. Soc.* 1999, 146, 392.
[68] Abdullah, M., K. Okuyama, I.W. Lenggoro, and S. Taya, *J Non-cryst. Solids.* 2005, 351, 697.
[69] Lee, S., H. Kim, S. Byeon, J. Park, and D. Kims, *Ind. Eng. Chem. Res* 2005, 44, 4300.
[70] Zhang, Z., Y. Wang, Y. Du, and F. Li, *J Rare Earth.* 2005, 23, 401.
[71] Zhang, Z. and Y. Wang, *Mater. Sci. Forum.* 2005, 475-479, 1701.
[72] Kuo, K., S. Lee, S. Chen, B. Cheng, H. Lu, D. Liu, and C. Ting, *J Phys. Chem. Solids* 2008, 69, 446.
[73] Zhou, Y., J. Lin, M. Yu, and S. Wang, *J Alloys Compd* 2004, 375, 93¨C97.
[74] Li, F., L. Hu, Z. Li, and X. Huang, *J Alloy. Compd.* 2008, 465, L14.
[75] Xu, Y., Z. Ren, G. Cao, W. Ren, K. Deng, and Y. Zhong, *Mater. Lett.* 2008, 62, 4525.
[76] Abdullah, M., K. Okuyama, I. Lenggoro, and S. Taya, *J Non-cryst. Solids.* 2005, 351, 697.
[77] Stevels, A. and A. Schrama-de Pauw, *J Lumin.* 1976, 14, 147.
[78] Smets, B. and J. Verlijsdonk, *Mater. Res. Bull.* 1986, 21, 1305.
[79] Smets, B., J. Rutten, G. Hoeks, and J. Verlijsdonk, *J Electrochem. Soc.* 1989, 136, 2119.
[80] Zhang, Z. and Y. Wang, *Mater. Lett.* 2007, 61, 4128.
[81] Boolchand, P., K. Mishra, M. Raukas, A. Ellens, and P. Schmidt, *Phys. Rev. B* 2002, 66, 134429.
[82] Mishra, K., M. Raukas, A. Ellens, and K. Johnson, *J Lumin.* 2002, 96, 95.
[83] Ronda, C.R. and B.M.J. Smets, *J Electrochem. Soc.* 1989, 136, 570.
[84] Zhang, Z., Y. Wang, and X. Li, *J Alloy. Compd.* 2009, 478, 801.

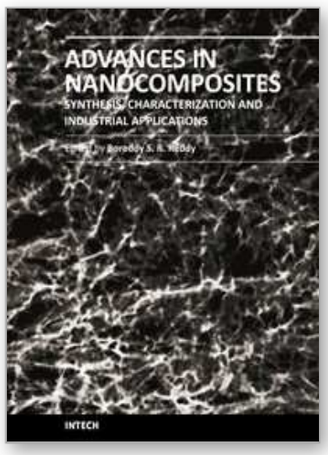

Advances in Nanocomposites - Synthesis, Characterization and Industrial Applications

Edited by Dr. Boreddy Reddy

ISBN 978-953-307-165-7
Hard cover, 966 pages
Publisher InTech
Published online 19, April, 2011
Published in print edition April, 2011

Advances in Nanocomposites - Synthesis, Characterization and Industrial Applications was conceived as a comprehensive reference volume on various aspects of functional nanocomposites for engineering technologies. The term functional nanocomposites signifies a wide area of polymer/material science and engineering, involving the design, synthesis and study of nanocomposites of increasing structural sophistication and complexity useful for a wide range of chemical, physicochemical and biological/biomedical processes. "Emerging technologies" are also broadly understood to include new technological developments, beginning at the forefront of conventional industrial practices and extending into anticipated and speculative industries of the future. The scope of the present book on nanocomposites and applications extends far beyond emerging technologies. This book presents 40 chapters organized in four parts systematically providing a wealth of new ideas in design, synthesis and study of sophisticated nanocomposite structures.

How to reference

In order to correctly reference this scholarly work, feel free to copy and paste the following:

Yuhua Wang, Qizheng Dong, Zhaofeng Wang and Xue Yu (2011). Synthesis of Nanosized Luminescent Materials and Their Photoluminescence under VUV Excitation, Advances in Nanocomposites - Synthesis, Characterization and Industrial Applications, Dr. Boreddy Reddy (Ed.), ISBN: 978-953-307-165-7, InTech, Available from: http://www.intechopen.com/books/advances-in-nanocomposites-synthesis-characterization-and-industrial-applications/synthesis-of-nanosized-luminescent-materials-and-their-photoluminescence-under-vuv-excitation

INTECH
open science | open minds

InTech Europe
University Campus STeP Ri
Slavka Krautzeka 83/A
51000 Rijeka, Croatia
Phone: +385 (51) 770 447
Fax: +385 (51) 686 166
www.intechopen.com

InTech China
Unit 405, Office Block, Hotel Equatorial Shanghai
No.65, Yan An Road (West), Shanghai, 200040, China
中国上海市延安西路65号上海国际贵都大饭店办公楼405单元
Phone: +86-21-62489820
Fax: +86-21-62489821

IntechOpen